10 January 2025, Preprint v1 · CC-BY 4.0

Research Article

Drift-Cyclotron Loss-Cone Instability in 3D Simulations of a Sloshing-Ion Simple Mirror

Aaron Tran[1], Samuel J. Frank[2], Ari Y. Le[3], Adam J. Stanier[3], Blake A. Wetherton[3], Jan Egedal[1], Douglass A. Endrizzi[1], Robert W. Harvey[4], Yuri V. Petrov[4], Tony M. Qian[5], Kunal Sanwalka[1], Jesse Viola[2], Cary B. Forest[1], Ellen G. Zweibel[6]

1. Department of Physics, University of Wisconsin–Madison, Madison, United States; 2. Realta Fusion; 3. Los Alamos National Laboratory, Los Alamos, United States; 4. CompX (United States), Dallas, United States; 5. Princeton Plasma Physics Laboratory, Plainsboro Center, United States; 6. Department of Astronomy, University of Wisconsin–Madison, Madison, United States

The kinetic stability of collisionless, sloshing beam-ion (45° pitch angle) plasma is studied in a 3D simple magnetic mirror, mimicking the Wisconsin High-temperature superconductor Axisymmetric Mirror (WHAM) experiment. The collisional Fokker-Planck code CQL3D-m provides a slowing-down beam-ion distribution to initialize the kinetic-ion/fluid-electron code Hybrid-VPIC, which then simulates free plasma decay without external heating or fueling. Over $1{-}10\ \mu\mathrm{s}$, drift-cyclotron loss-cone (DCLC) modes grow and saturate in amplitude. DCLC scatters ions to a marginally-stable distribution with gas-dynamic rather than classical-mirror confinement. Sloshing ions can trap cool (low-energy) ions in an electrostatic potential well to stabilize DCLC, but DCLC itself does not scatter sloshing beam-ions into said well. Instead, cool ions must come from external sources such as charge-exchange collisions with a low-density neutral population. Manually adding cool $\sim 1\ \mathrm{keV}$ ions improves beam-ion confinement $\sim 2{-}5\times$ in Hybrid-VPIC simulations, which qualitatively corroborates measurements from real mirror devices with sloshing ions.

Corresponding author: Aaron Tran, atran@physics.wisc.edu

doi.org/10.32388/6MKS9W

1. Introduction

The Wisconsin High-temperature superconductor Axisymmetric Mirror (WHAM) is a new laboratory experiment that confines hot plasmas in a magnetic mirror with a maximum field of 17 T on axis, generated by high-temperature superconductors (HTS)[1]. For WHAM and future mirror devices[2][3][4] to succeed, both fluid and kinetic plasma instabilities must be quelled.

A kinetic instability of particular concern is the drift-cyclotron loss-cone (DCLC) instability[5][6]. DCLC comprises a spectrum of ion Bernstein waves, coupled to a collisionless drift wave, that is excited by a spatial density gradient ∇n and a loss-cone ion velocity distribution. In a magnetized plasma column, DCLC appears as an electrostatic wave that propagates around the column's azimuth in the ion diamagnetic drift direction, perpendicular to both $\mathbf{B}$ and ∇n. DCLC can be unstable solely due to ∇n when the gradient length scale $n/(\nabla n)$ is of order the ion Larmor radius ρ_{i}, even for distributions without a loss cone (e.g., Maxwellians), in which case it may be called drift-cyclotron instability[7]. In this manuscript, we call both drift-cyclotron and drift-cyclotron loss-cone modes by "DCLC" for simplicity.

Many mirror devices have measured electric and/or magnetic fluctuations at discrete ion cyclotron harmonics having properties consistent with DCLC. These devices include PR-6[8][9], PR-8[10], 2XIIB[11], TMX and TMX-U[12][13][14], LAMEX[15], MIX-1[16][17][18][19], GAMMA-6A[20], and GDT[21][22]. Experiments on these devices showed that DCLC may be partly or wholly stabilized by filling the ions' velocity-space loss cone via axial plasma stream injection[9][11][12][13][14][23][24], filling the loss cone via angled neutral beam injection, which creates a non-monotonic axial potential that traps cool ions[22][25][26][27][28][29], decreasing ∇n with respect to the ion Larmor radius ρ_{i}[15], and bounce-resonant electron Landau damping[16]. Other effects theoretically calculated to modify and/or help stabilize DCLC include finite plasma beta[30], radial ambipolar electric fields[31][32], and low-frequency external electric fields[33][34].

WHAM's plasma column is a few to several ion Larmor radii (ρ_{i}) in width and so may excite DCLC. How will DCLC appear in WHAM; i.e., what will be its azimuthal mode number, oscillation frequency, and amplitude? Sloshing ions, injected at 45° pitch-angle, helped to suppress DCLC in TMX-U endplugs and will also be deployed on WHAM; to what extent can sloshing ions similarly suppress DCLC in WHAM? In general, how should WHAM's plasma properties be tuned to suppress DCLC? These questions have been addressed to varying degrees, for previous devices, via linear theory[5][6][30][35][36][37][38][39][40][41], quasi-linear theory[42][43], non-linear theory[33][44][45], and 1D and 2D kinetic computer simulations[37][38][46][47][48][49].

Here, we address the aforementioned questions using 3D full-device computer simulations of DCLC growth and saturation in a hybrid (kinetic ion, fluid electron) plasma model. Our simulation accounts for many physical effects relevant to WHAM—magnetic geometry, beam-ion distributions, both radial and axial electrostatic potentials, and diamagnetic field response—to obtain a fuller and more integrated kinetic model than was possible decades ago.

In §2 we describe our simulation methods and parameters; of note is the coupling of a collisional Fokker-Planck transport model to a collisionless hybrid kinetic-ion simulation model. In §3.1 to §3.3, we characterize three fiducial simulations evolved to 6 μs that have reached a steady-state decay. The main instability in all simulations is described and identified as DCLC, with the aid of an approximate linear dispersion relation for electrostatic waves in an inhomogeneous, low-β planar-slab plasma. In §3.4, particle confinement is shown to obey a "gas dynamic" rather than "collisionless mirror" scaling with mirror ratio and device length. In §4 we survey well-known ways to stabilize DCLC that may be relevant to WHAM and next-step mirror devices. We particularly focus on the experimentally-tested method of DCLC stabilization via trapped cool ions, and we show that adding cool ions can improve beam-ion confinement by a factor of 2–$5\times$ in our simulations. Finally, §5 concludes.

2. Methods

2.1. Simulation Overview

We simulate freely-decaying plasma in a 3D magnetic mirror made of one central cell and two expanders (Figure 1, left column). Three magnetic-field configurations are used, labeled by vacuum mirror ratio $R_\mathrm{m} = \{20, 41, 64\}$, to span WHAM's operating range. WHAM's magnetic field is created by two HTS coils at $z = \pm 98$ cm and two copper coils at $z = \pm 20$ cm[1]. When both HTS and copper coils are fully powered, the magnetic field on axis varies between $B \approx 17.3$ T at the mirror throats to 0.86 T at the device's center ($R_\mathrm{m} = 20$). When the copper coils are partly powered, B on axis ranges between 17.2 to 0.414 T ($R_\mathrm{m} = 41$). When the copper coils are unpowered, B on axis ranges between 17.1 to 0.267 T ($R_\mathrm{m} = 64$).

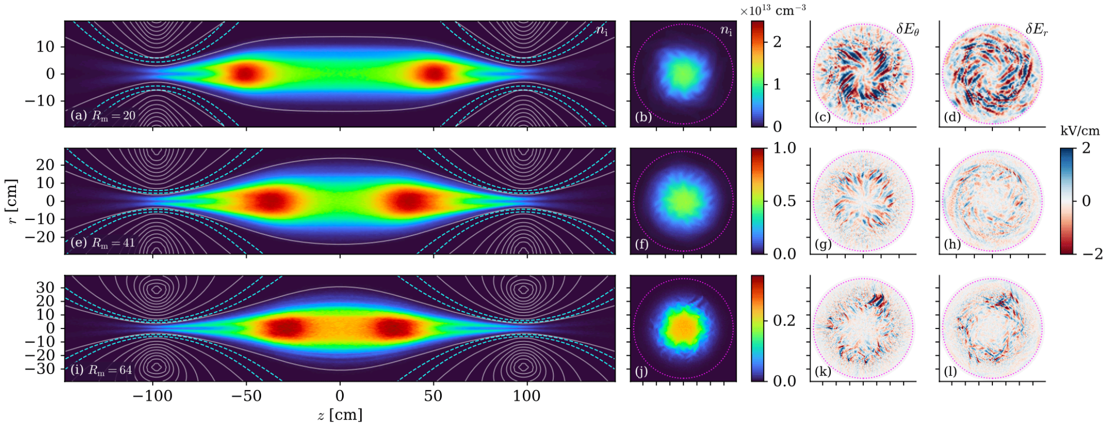

Figure 1. 2D images of ion density and electric field fluctuations at $t \approx 6\tau_{bounce} \approx 6\mu s$, for three simulations with varying vacuum mirror ratio $R_{\mathrm{m}} = 20$ (top row), 41 (middle row), 64 (bottom row). (a): ion density n_i in units of $10^{13}\mathrm{cm}^{-3}$, 2D slice at $y = 0$ in (x, y, z) coordinates. White lines trace vacuum magnetic fields; dashed cyan lines trace hyperresistive dampers and conducting $E = 0$ regions (see text). (b): like (a), but 2D slice at the mirror's mid-plane $z = 0$ showing coherent flute-like fluctuations at the plasma edge. (c): azimuthal electric field fluctuation δE_θ in kV/cm; magenta dotted line traces radial conducting boundary. (d): like (c), but radial fluctuation δE_r. Middle row (e)-(h) and bottom row (i)-(l) are organized like panels (a)-(d). Aspect ratio is distorted in left column (a),(e),(i); aspect ratio is to scale in all other panels.

Our simulations are performed with the code Hybrid-VPIC[1][50][51], which models ion kinetics using the particle-in-cell (PIC) method and models electrons as a neutralizing fluid. Ions are advanced using a Boris pusher[51]. Electric and magnetic fields $\mathbf{E}$, $\mathbf{B}$ are evolved on a rectilinear Cartesian (x, y, z) mesh. Particle-mesh interpolation uses a quadratic-sum shape[50]. The magnetic field is advanced using Faraday's Law, $\partial \mathbf{B}/\partial t = -c\nabla \times \mathbf{E}$, with a 4th-order Runge-Kutta scheme. The electric field is passively set by a generalized Ohm's law without electron inertia:

$$\mathbf{E} = -\frac{\mathbf{V}_i \times \mathbf{B}}{c} + \frac{\mathbf{j} \times \mathbf{B}}{e n_e c} - \frac{\nabla P_e}{e n_e} + \eta \mathbf{j} - \eta_H \nabla^2 \mathbf{j}\,, \tag{2.1}$$

assuming both $\mathbf{j} = c\nabla \times \mathbf{B}/(4\pi)$ and $n_e = n_i$. Here n_i and n_e are ion and electron number densities, $\mathbf{V}_i$ is bulk ion velocity, P_e is scalar electron presure, $\mathbf{j}$ is current density, η is resistivity, η_H is hyper-resistivity, c is the speed of light, and e is the elementary charge. Gaussian CGS units are used in this manuscript unless otherwise stated.

Coulomb collisions are neglected because the ion-ion deflection and ion-electron drag timescales in WHAM are of order $\mathcal{O}(\mathrm{ms})$, longer than our simulation durations $\sim 1\text{–}10\ \mu$s.

A density floor of $n_e \geq \{15, 6, 1.5\} \times 10^{11}\ \mathrm{cm}^{-3}$, for the $R_m = \{20, 41, 64\}$ simulations respectively, is applied in the Hall and ambipolar (pressure gradient) terms of Equation 2.1 to prevent division-by-zero in vacuum and low-density regions surrounding the plasma. The density floor is set low enough to obtain the electrostatic potential drop from $z = 0$ out to the mirror throats at $z = \pm 98\ \mathrm{cm}$, but the remaining potential drop from throat into expanders is not captured.

We set the resistivity $\eta = 0$ and the hyper-resistivity $\eta_H = 2.75 \times 10^{-14}\ \mathrm{s\,cm}^2$. Hyper-resistivity is used solely to damp high-frequency whistler noise at the grid scale $k \sim \pi/\Delta z$; η_H does not represent any sub-grid physics of interest to us. The hyper-resistive $\mathbf{E}$ is included in the ion push, since it is not used to model electron-ion friction.[2]

2.2. *Simulation Geometry*

The simulation domain for the $R_m = 20$ case is a rectangular box with extent $L_x = L_y = 39.2\ \mathrm{cm}$ and $L_z = 294\ \mathrm{cm}$. The box is decomposed into a $96^2 \times 384$ Cartesian (x, y, z) mesh with cell dimensions $\Delta x = \Delta y = 0.41\ \mathrm{cm}$ and $\Delta z = 0.77\ \mathrm{cm}$. For analysis and discussion, we project data into usual cylindrical coordinates (r, θ, z). For the $R_m = 41$ and 64 cases, the domain is enlarged to $L_x = L_y = 58.8$ and $78.4\ \mathrm{cm}$ while preserving the mesh cell shape, so the number of mesh points is $144^2 \times 384$ and $192^2 \times 384$ respectively. The domain extent truncates the expanders at $z = \pm 147\ \mathrm{cm}$, unlike the real experiment, wherein a set of staggered biasable rings collects escaping plasma at $z \sim 190$–$210\ \mathrm{cm}$[1][52].

The overall simulation timestep $\Delta t = 7.3 \times 10^{-11}\ \mathrm{s}$. The magnetic-field advance is sub-cycled $\{100, 250, 1000\}$ times within Δt, for $R_{\mathrm{m}} = \{20, 41, 64\}$ respectively, to satisfy the whistler wave's stiff CFL criterion in high-field, low-density regions near the mirror throats.

Hyper-resistivity η_{H} acts like smoothing and removes grid-scale numerical noise on the whistler-wave dispersion branch, which would otherwise be undamped in the absence of resistivity or hyper-resistivity. The value of η_{H} must be kept small enough to not artificially smooth real physical phenomena. The hyper-resistive diffusion timescale estimated as $\left[\eta_{\mathrm{H}} c^2/(4\pi L^4)\right]^{-1}$ for an arbitrary lengthscale L is $1.4 \times 10^{-8}\ \mathrm{s}$ for the transverse grid scale $L \sim \Delta x$; it is $600\ \mu\mathrm{s}$ for the ion skin depth $L \sim c/\omega_{\mathrm{pi}} \sim 6\ \mathrm{cm}$ with $n \sim 3 \times 10^{13}\ \mathrm{cm}^{-3}$. We cannot make η_{H} much larger because the scale separation between grid noise and physical phenomena is small; high-m kinetic modes lie below the ion skin depth. In Appendix A, we present density fluctuation properties from a three-point scan of

η_{H}; some details (e.g., spectral bandwidth) are altered, but the main conclusions regarding DCLC are not too sensitive to our chosen value of η_{H}.

Particle and field boundary conditions are imposed as follows. A conducting radial sidewall is placed at $r = 0.47 L_x$, which is in physical units $\{18.4, 27.6, 36.8\}$ cm for $R_{\mathrm{m}} = \{20, 41, 64\}$ respectively. A conducting axial sidewall is placed at $z = 0.485 L_z = \pm 143$ cm. The HTS coils are also surrounded by both conducting and hyper-resistive wrapper layers (Figure 1, left column, dashed cyan curves). Within the wrapper layer (between nested dashed cyan curves), the grid-local value of η_{H} used in Ohm's Law (Equation 2.1) is increased $30\times$ to help suppress numerical noise in high-field, low-density regions. The "conducting" boundary is enforced by setting $\boldsymbol{E} = 0$ on the mesh, which disables $\boldsymbol{B}$ field evolution. Bound charge and image currents within conducting surfaces are not explicitly modeled. Particles crossing the Cartesian domain boundaries ($x = \pm L_x/2$, $y = \pm L_y/2$, $z = \pm L_z/2$) are removed from the simulation. Boundary conditions are applied to $\boldsymbol{E}$ at cell centers in a nearest-grid-point manner, which may contribute to mesh imprinting; boundaries might be improved with a cut-cell algorithm or simply higher grid resolution in future work.

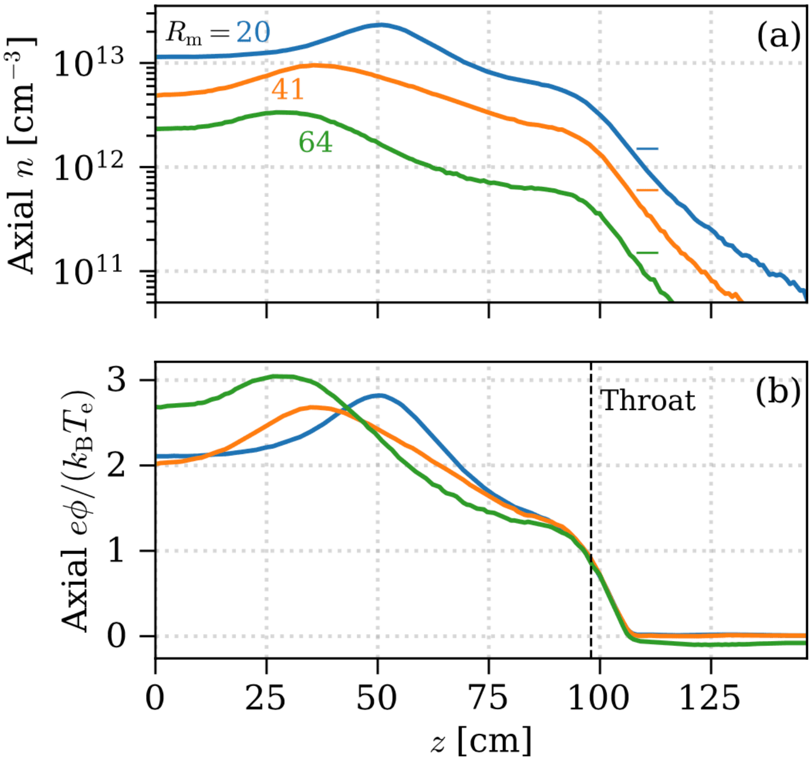

Figure 2. (a) Density on axis, at $r = 0$, extending from $z = 0$ cm (mid-plane) to expander end-walls $z = 147$ cm, measured at $t = 6\tau_{\mathrm{bounce}} \approx 6\mu s$. Blue, orange, green curves show simulations with vacuum $R_{\mathrm{m}} = 20, 41, 64$ respectively. Horizontal dashes near $z = 110$ cm show density floor for Ohm's law calculation of $\mathbf{E}$. (b) Electrostatic potential $e\phi$ in units of electron temperature for the same three simulations (color). Vertical dotted line at $z = 98$ cm marks location of HTS mirror throats. The potential falls to zero near $z = 110$ cm, which corresponds to the location of the density floor marked by dashes in (a).

2.3. Plasma Parameters

We model a fully-ionized deuteron-electron plasma ($m_{\mathrm{i}} = 3.34 \times 10^{-24}$ g) with typical ion density $n_{\mathrm{i}} \sim 10^{12}$ to 10^{13} cm^{-3} and temperature $T_{\mathrm{i}} \sim 5$ to 13 keV in the mirror's central cell. The ion velocity distribution is a beam slowing-down distribution with pitch angle $\cos^{-1}(v_{\parallel}/v) \sim 45^{\circ}$ at the mirror mid-plane ($z = 0$) to mimic WHAM's angled neutral beam injection (NBI). The beam path is centered on axis ($r = 0$).

The ions' spatial and velocity distributions are obtained from the bounce-averaged, zero-orbit-width, collisional Fokker-Planck code CQL3D-m[4][53]. We initialize the CQL3D-m simulations with a $1.5 \times 10^{13}\ \mathrm{cm}^{-3}$ plasma at low temperature $T_i = T_e = 250\ \mathrm{eV}$, mimicking the initial electron-cyclotron heating (ECH) breakdown of a gas puff in WHAM.[3] The plasma is simulated by CQL3D-m on 32 flux surfaces spanning normalized square root poloidal flux, $\sqrt{\psi_n} = 0.01\text{–}0.9$, as it is fueled and heated with a realistic 25 keV neutral beam operating at the experimental parameters. No heating or fueling sources other than the neutral beam are included. The velocity-space grid has 300 points in total momentum-per-rest-mass $p/(mc)$, and either 256 or 300 points in pitch angle. The total-momentum grid is not linearly spaced, but instead geometrically scaled at low energies to cover the ion distribution function. The pitch-angle grid is uniformly spaced. CQL3D-m uses a timestep of $0.0625\ \mathrm{ms}$, advancing ions and electrons simultaneously. The neutral beam deposition profile is updated after each timestep using CQL3D-m's internal FREYA neutral-beam Monte-Carlo solver. To include the diamagnetic $\mathbf{B}$-field response to the plasma pressure, the CQL3D-m solve is iterated with the MHD equilibrium solver Pleiades[4][54], with improvements to treat pressure-anisotropic equilibria[55]. CQL3D-m and Pleiades are coupled using a customized version of the Integrated Plasma Simulator framework[56]. The diamagnetic field is updated in CQL3D-m every $1\ \mathrm{ms}$.

We perform separate CQL3D-m runs for each of the $R_\mathrm{m} = \{20, 41, 64\}$ cases. In each case, the NBI power is adjusted in 100 kW increments, until the 1 MW maximum input power of the experiment is reached or a mirror instability driven β limit occurs[57]. The $R_\mathrm{m} = \{20, 41, 64\}$ cases operate with NBI power $\{200, 400, 1000\}\ \mathrm{kW}$ respectively. The CQL3D-m/Pleiades loop is run for the duration of a laboratory shot, to $20\ \mathrm{ms}$ (which is $t = 0$ for Hybrid-VPIC). At each end of the CQL3D-m run, all three cases have plasma $\beta \sim 0.60$. The low $R_\mathrm{m} = 20$ (high $\mathbf{B}$-field) case achieves the highest plasma density $1\text{–}3 \times 10^{13}\ \mathrm{cm}^{-3}$ on axis in the central cell (Figure 2(a)). The ions have $T_\mathrm{i} = \{13, 11, 11\}\ \mathrm{keV}$ at the origin $(r, z) = (0, 0)$ in the $R_\mathrm{m} = \{20, 41, 64\}$ cases respectively. Of note, the $R_\mathrm{m} = 64$ case has a cooler ion plasma temperature $T_\mathrm{i} \sim 5\ \mathrm{keV}$ at the plasma's radial edge, whereas the lower R_m (higher field) CQL3D-m simulations maintain $T_\mathrm{i} \sim 10\ \mathrm{keV}$ from the axis $r = 0$ to the edge. This is a result of the larger cool thermal ion population that is trapped by the sloshing-ion distribution in the $R_\mathrm{m} = 64$ case.

The CQL3D-m bounce-averaged distribution function at the mirror's mid-plane ($z = 0$) is mapped on Liouville characteristics to all (r, z) and read into Hybrid-VPIC as an initial condition for both real-and velocity-space ion distributions. The CQL3D-m ion radial density profile n is extrapolated from $\sqrt{\psi_n} = 0.9$ to 1 as

$$n(\psi_n) = \cos^2\left[\frac{\pi}{2}\left(\frac{\psi_n - 0.81}{1 - 0.81}\right)\right]. \tag{2.2}$$

where $\psi_n = \psi/\psi_{\text{limiter}}$, $\psi = \int 2\pi B r \mathrm{d}r$, and $\psi_{\text{limiter}} = 2.32 \times 10^6\ \mathrm{G\,cm}^2$. This sets the plasma's initial extent. No limiter boundary condition is implemented in the Hybrid-VPIC simulation.

Electron velocity distributions and the electrostatic potential ϕ are also solved in CQL3D-m via an iterative technique[55], but neither are directly input to Hybrid-VPIC's more-approximate fluid electron model. Instead, we set the Hybrid-VPIC electron temperature $T_{\mathrm{e}} = \{1.25, 1.5, 1.0\}$ keV in the $R_{\mathrm{m}} = \{20, 41, 64\}$ cases respectively, with T_{e} values taken from the CQL3D-m simulation at $(r, z) = (0, 0)$. All simulations use an isothermal equation of state, so T_{e} is constant in space and time.

We use $N_{\mathrm{ppc}} = 8000$ ion macroparticles per cell, pinned to a reference density $3 \times 10^{13}\ \mathrm{cm}^{-3}$, so the initial number of particles is highest at the beam-ion turning points and lower elsewhere; all particles have equal weight (or charge) in the PIC algorithm.

We initialize particles on their gyro-orbits with random gyrophase; this spatially smooths the initial radial distribution of plasma density and pressure, as compared to the CQL3D-m density distribution which places particles at their gyrocenters. The initial plasma in Hybrid-VPIC thus has non-zero initial azimuthal diamagnetic drift and hence net angular momentum. We also initialize the diamagnetic field from Pleiades in the Hybrid-VPIC simulation, though our initial plasma does not satisfy this equilibrium due to the Larmor radius offsets from particle gyrocenters. Thus, the Hybrid-VPIC simulation evolves towards a new pressure equilibrium as the plasma settles into steady state.

With the ion distributions specified, let us define thermal length and time normalizations. The angular ion cyclotron frequency $\Omega_{\mathrm{i0}} = eB(z=0)/(m_{\mathrm{i}}c)$ at the mirror mid-plane. The ion bounce (or, axial-crossing) time $\tau_{\text{bounce}} = L_{\mathrm{p}}/v_{\mathrm{ti0}} \approx 1\ \mu$s using the mirror's half length $L_{\mathrm{p}} = 98$ cm and a reference ion thermal velocity $v_{\mathrm{ti0}} = \sqrt{T_{\mathrm{i0}}/m_{\mathrm{i}}} = 0.00327c = 9.8 \times 10^7$ cm/s, with $T_{\mathrm{i0}} = 20$ keV and c the speed of light. Though the CQL3D-m initialized ions have $T_{\mathrm{i}} \sim 10\,\mathrm{keV}$, our chosen v_{ti0} approximates $v_\perp \sim v_\parallel \sim (25\ \mathrm{keV})/\sqrt{2}$ for the beam-ion distribution's primary and secondary peaks. We also define a reference ion Larmor radius $\rho_{\mathrm{i0}} = v_{\mathrm{ti0}}/\Omega_{\mathrm{i0}}$ at the mirror mid-plane. Tables 1 and 2 summarize physical and numerical parameters, respectively, for our three fiducial simulations.

R_m	L_p	$B(z = 0)$	f_ci0	v_ti0	ρ_i0	T_e	**Core T_i at** $0\ \mu\mathrm{s}$	**Edge $T_{\mathrm{i}\perp}$ at** $6\ \mu\mathrm{s}$	**Edge $T_{\mathrm{i}\parallel}$ at** $6\ \mu\mathrm{s}$
20	98 cm	0.86 T	6.5 MHz	980 km /s	2.37 cm	1.25 keV	13 keV	8.4 keV	17.1 keV
41	$\cdots$	0.41	3.1	$\cdots$	4.94	1.5	11	6.5	13.1
64	$\cdots$	0.27	2.0	$\cdots$	7.64	1.0	11	6.4	8.0

Table 1. Physical parameters for fiducial simulations, labeled by vacuum mirror ratio R_m. The ion cyclotron frequency f_ci0 is $\Omega_\mathrm{i0}/(2\pi)$ and ion Larmor radius ρ_i0 is $v_\mathrm{ti0}/\Omega_\mathrm{i0}$. Ions are deuterons. Core T_i at $0\ \mu\mathrm{s}$ is measured at the origin $(r, z) = (0, 0)$.

R_m	L_x	L_z	Δx	Δz	Δt	**Subcycles**	η	η_H
20	39.2 cm	294 cm	0.41 cm	0.77 cm	7.3×10^{-11} s	100	0 s	2.75×10^{-14} s cm^2
41	58.8	$\cdots$	$\cdots$	$\cdots$	$\cdots$	250	$\cdots$	$\cdots$
64	78.4	$\cdots$	$\cdots$	$\cdots$	$\cdots$	1000	$\cdots$	$\cdots$

Table 2. Numerical parameters for fiducial simulations, labeled by vacuum mirror ratio R_m.

3. Results

3.1. Space, Velocity Structure of Steady-State Decay

At the start of each simulation, the plasma relaxes from its initial state over $\sim 1\text{–}3\tau_\mathrm{bounce}$; the diamagnetic field response is changed, short-wavelength electrostatic fluctuations occur at the plasma edge, and plasma escapes from the central cell into the expanders. The plasma reaches a steady-state decay by $t = 6\tau_\mathrm{bounce}$ for all R_m simulations. At this time, (i) the particle loss time $\tau_p = n/(\mathrm{d}n/\mathrm{d}t)$ is roughly constant and exceeds the ion bounce time ($\tau_p \gg \tau_\mathrm{bounce}$), (ii) the plasma beta $\beta_i = 8\pi P_i/B^2 \sim 0.1$ to within a factor of two at the origin $(r, z) = (0, 0)$, with P_i the total ion pressure, (iii) the combined vacuum and diamagnetic fields attain a mirror ratio $R_m = 21, 45, 69$ somewhat higher than the respective vacuum values $R_m = 20, 41, 64$.

Figure 1 shows the plasma's overall structure at $t = 6\tau_{\mathrm{bounce}}$ for each of the vacuum $R_m = 20, 41, 64$ simulations. Flute-like, electrostatic fluctuations at the plasma's radial edge are visible in $z = 0$ slices of ion density and electric fields, with the strongest and most coherent fluctuations for the $R_m = 20$ case. In the left-most panels (a), (e), (i), the axial outflow at $|z| \gtrsim 70\ \mathrm{cm}$ is split about $r = 0$, so more plasma escapes from the radial edge $r > 0$ than the core $r \sim 0$. In the right-most panels (d), (h), (l), the radial electric field fluctuation $\delta E_r = E_r - \langle E_r \rangle_\theta$, where $\langle \cdots \rangle_\theta$ represents an average over the azimuthal coordinate to subtract the plasma's net radial potential. The azimuthal fluctuation δE_θ in panels (c), (g), (k) is defined similarly. The transverse magnetic fluctuations δB_r and δB_θ have small amplitudes $\lesssim 10^{-3} B(z = 0)$, whereas the electric fluctuations δE_r and δE_θ are of order $0.1 v_{\mathrm{ti0}} B(z = 0)/c$, corresponding to motional flows at thermal speeds. We therefore neglect electromagnetic fluctuations and focus solely on the azimuthal, electrostatic mode visible in Figure 1.

Figure 2a shows the ion density on axis, with horizontal dashes marking the density floor imposed in Ohm's Law (Equation 2.1). Figure 2b shows that the density floor truncates the axial electrostatic potential at $z \approx 110\ \mathrm{cm}$, so the full potential drop from the mirror throat to the domain's z boundary is not captured in our simulation. In any case, plasma outflow in the expanders is not well modeled by our electron closure, as the outflow is far from thermal equilibrium[58]. In this manuscript, we restrict our attention to central-cell plasma behavior that we suppose to be unaffected by the expanders.

Figure 3 shows initial ion velocity distributions, as imported into Hybrid-VPIC from CQL3D-m, at the center of the mirror cell: $z \in (-5.9, 5.9)\ \mathrm{cm}$ for all simulations. Panels (a)–(d) sample ions from the plasma's radial edge: $r \in [5.9, 11.8)\ \mathrm{cm}$ for $R_{\mathrm{m}} = 20$; $r \in [11.8, 23.5)\ \mathrm{cm}$ for $R_{\mathrm{m}} = 41$; $r \in [14.7, 29.4)\ \mathrm{cm}$ for $R_{\mathrm{m}} = 64$. Panel (e) samples ions from the plasma's core: $r \in [0, 2.9)\ \mathrm{cm}$ for $R_{\mathrm{m}} = 20$; $r \in [0, 5.9)\ \mathrm{cm}$ for $R_{\mathrm{m}} = 41$; $r \in [0, 7.4)\ \mathrm{cm}$ for $R_{\mathrm{m}} = 64$. Panels (f)-(j) shows ion distributions, selected from the same axial and radial regions as the top row, after the simulation has reached $t = 6\tau_{\mathrm{bounce}} \approx 6\ \mu\mathrm{s}$. Ions diffuse mostly in $v_\perp$; their distribution is continuous and nearly flat across the velocity-space loss-cone boundary. The reduced distribution $F(v_\perp) = \int f \mathrm{d}v_\parallel$ has relaxed to a monotonically decreasing shape, $\mathrm{d}F/\mathrm{d}v_\perp < 0$, at the plasma edge (Figure 3f); however, the core plasma maintains $\mathrm{d}F/\mathrm{d}v_\perp > 0$ at low $v_\perp$ (Figure 3j). Some distribution function moments will be used in later discussion. We define $\boldsymbol{B}$-perpendicular and parallel temperatures $T_{\mathrm{i}\perp} \equiv (1/2) \int m_{\mathrm{i}} v_\perp^2 f \mathrm{d}\boldsymbol{v}$ and

$T_{\mathrm{i}\|} \equiv \int m_{\mathrm{i}} v_{\|}^{2} f \mathrm{d}\boldsymbol{v}$ so that $T_{\mathrm{i}} = (2T_{\mathrm{i}\perp} + T_{\mathrm{i}\|})/3$; temperature values for the edge ion distributions at $t = 6\,\tau_{\mathrm{bounce}}$ Figure 3(f–i) are given in Table 1.

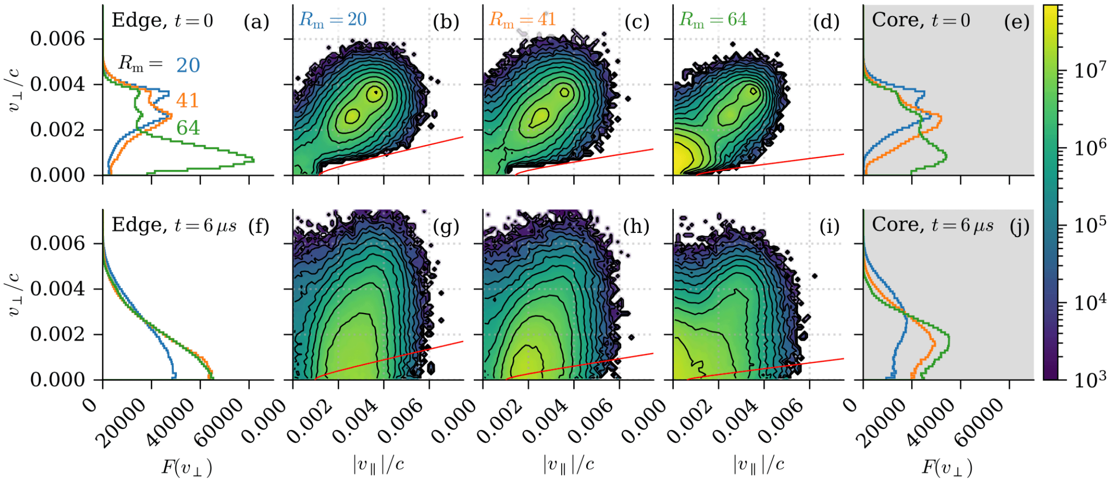

Figure 3. Initial (top row) and relaxed (bottom row) ion velocity distributions at the plasma edge, in three simulations. Edge ion distributions smooth and flatten in $v_\perp$ as the simulation evolves, with a stronger effect for edge plasma as compared to core plasma. The loss cone is filled, and the distribution varies little across the loss-cone boundary. (a): reduced distribution $F(v_\perp)$ for simulations with vacuum $R_{\mathrm{m}} = 20$ (blue), 41 (orange), and 64 (green). Distribution is normalized so that $\int F(v_\perp) 2\pi v_\perp \mathrm{d}v_\perp = 1$. (b)-(d): 2D distributions $f(v_\perp, v_\|)$ for each of the three simulations shown in (a), normalized so that $\int f 2\pi v_\perp \mathrm{d}v_\perp \mathrm{d}v_\| = 1$. Red curves plot loss-cone boundary, with the effect of electrostatic trapping approximated using the on-axis Yushmanov potential well depth, measured to range between 0.4 to $1.9\mathrm{keV}$ in Hybrid-VPIC. (e): Like (a), but a “core” distribution centered on $r = 0$ for comparison to the “edge”. (f)-(j): like top row, but at later time $t = 6\mu s$ in the simulation. In all panels, velocities $v_\perp$, $v_\|$ are normalized to the speed of light c.

Figure 4 shows a 3D render of ion density in the $R_{\mathrm{m}} = 20$ simulation at $t = 6$ μs. The flute-like ($k_\| \sim 0$) nature of the edge fluctuations is apparent. An accompanying movie of the full time evolution from $t = 0$ to 6 μs is available in the online journal.

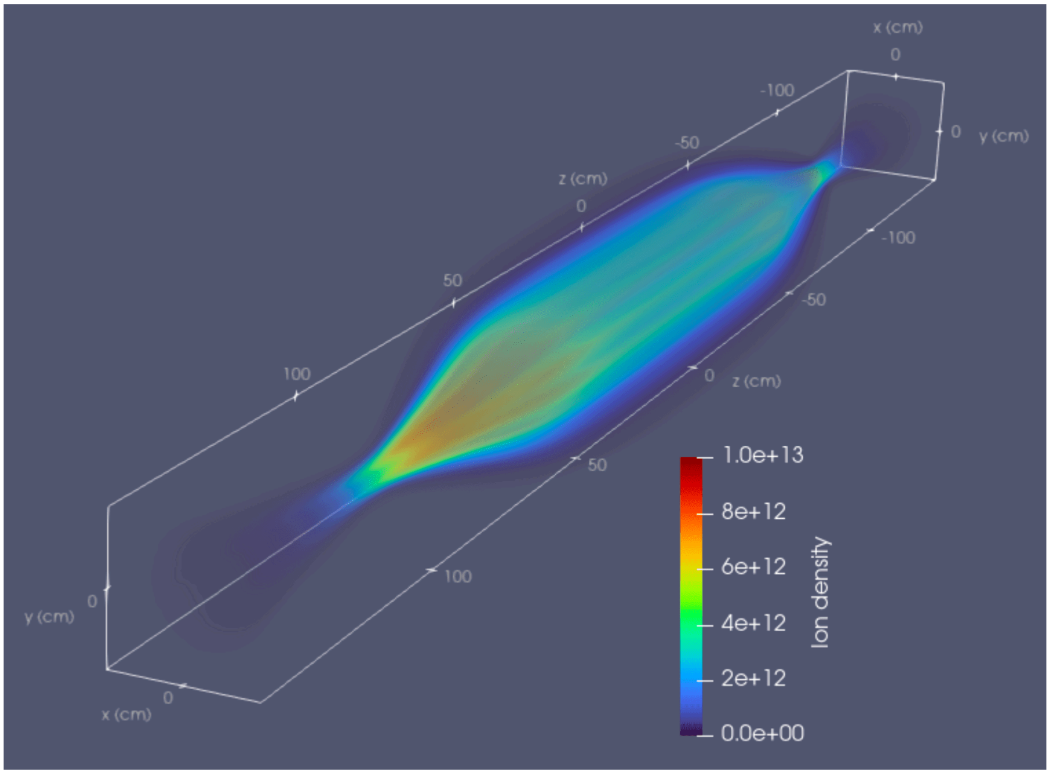

Figure 4. 3D rendering of ion density in $R_{\mathrm{m}} = 20$ simulation at $t = 6\mu\mathrm{s}$; colormap is ion density in units of cm^{-3}. An animated movie is available in the online journal. While the article is in review, the movie is also available at the corresponding author's website.

To summarize, Figures 1–4 show that at the plasma's radial edge, (i) flute-like electrostatic fluctuations appear, (ii) axial outflow and hence losses are enhanced relative to the plasma's core at $r \sim 0$, and (iii) ions diffuse in $v_\perp$ to drive $\mathrm{d}F/\mathrm{d}v_\perp < 0$. It is already natural to suspect that the electrostatic fluctuations diffuse ions into the loss cone and hence cause plasma to escape the mirror.

3.2. *Drift Cyclotron Mode Identification*

To establish the electrostatic mode's nature, we need to know plasma properties at the radial edge and the mode's wavenumber and frequency spectrum.

Figure 5 (left three columns) presents the radial structure of the ion density n_{i}, and the electrostatic fluctuation energy $\delta E_\theta^2 = \langle E_\theta^2 \rangle_\theta - \langle E_\theta \rangle_\theta^2$, at the mirror mid-plane $z = 0$. Figure 5 (right two columns) also presents Fourier spectra of density $\tilde{n}_{\mathrm{i}}(m, r)$ and electric component $\tilde{E}_\theta(m, r)$ as a function of azimuthal mode number m and radius r.

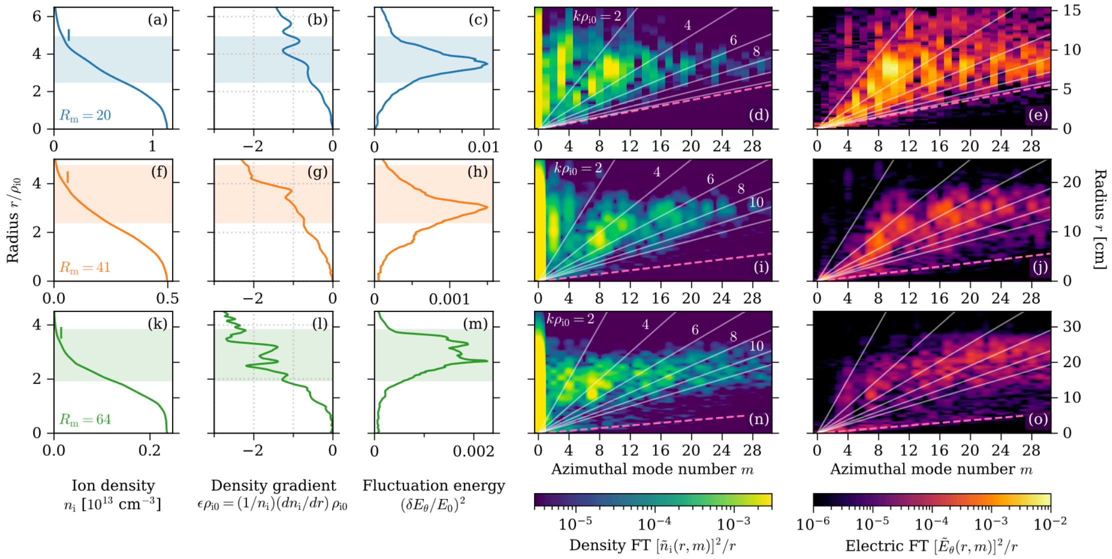

Figure 5. Radial structure of plasma at mid-plane $z = 0$ and at $t = 6\,\tau_\mathrm{bounce} \approx 6\mu$s, for simulations with vacuum $R_\mathrm{m} = 20$ (top row), 41 (middle row), 64 (bottom row). Left three columns show azimuth-averaged radial profiles of (a) ion density n_i, (b) ion density gradient $\epsilon\rho_{i0}$, (c) azimuthal electrostatic fluctuation energy δE_θ^2 , normalized to a reference field $E_0 = 20.8\mathrm{V/cm}$. Horizontal shaded bars contain the “edge” ion distributions from Figure 3. Vertical dashes in left-most column mark density floor for Equation 2.1. Right two columns (d)-(e) show azimuthal Fourier spectra of density $\tilde{n}_\mathrm{i}(r,m)$ and azimuthal electric field $\tilde{E}_\theta(r,m)$; Fourier transform maps $\theta \to m$, but radius r is not transformed. White rays mark azimuthal wavenumber $k\epsilon\rho_{i0} = 2, 4, 6, 8, 10, 12$, with $k = m/r$. Dashed pink ray is the maximum $k = \pi/\Delta r$ resolved by the spatial grid, taking $\Delta r = \sqrt{2}\Delta x$. Panels (f)-(j) and (k)-(o) are organized similarly.

The density gradient $\epsilon \equiv (\mathrm{d}n_\mathrm{i}/\mathrm{d}r)/n_\mathrm{i}$, in units of inverse ion Larmor radius ρ_{i0}^{-1}, is of order unity and increases with R_m (Figure 5(b),(g),(l)); equivalently, the plasma column radius is smaller in units of ρ_{i0} for larger R_m (despite the column’s larger physical extent).

The mode spectra of $\tilde{n}$ and $\tilde{E}_\theta$ suggest a partial decoupling of density and electric fluctuations (Figure 5, right two columns). In all simulations, low $m \sim 2$–4 density fluctuations are not accompanied by a strong E_θ signal (Figure 5, right two columns). The $R_\mathrm{m} = 20$ simulation shows a strong mode in both density and E_θ fluctuations at $m \approx 9$–10 and equivalent angular wavenumber $k\rho_{i0} \approx 2$–4 (Figure 5(d)-(e)). We identify this Fourier signal with phase-coherent fluting at the same m visible to the eye in Figure 1(b),(c). In contrast, the $R_\mathrm{m} = 41, 64$ simulations show a decoupling of density and E_θ fluctuations. The strongest density fluctuations reside at $r \sim 1{-}2\rho_{\mathrm{i}0}$, $m \sim 7{-}8$, and $k\rho_{\mathrm{i}0} \approx 2{-}6$ (Figure 5(i),(n)), whereas the electrostatic fluctuations reside at larger $r \sim 2{-}4\rho_{\mathrm{i}0}$, $m \sim 15$ -30, and $k\rho_{\mathrm{i}0} \sim 4{-}12$ (Figure 5(j),(o)).

The fluctuations have $k_\parallel \ll k_\perp$ and are thus flute-like, which we checked by plotting $\boldsymbol{E}$ in approximate flux-surface coordinates (not shown). Electric-field fluctuations terminate at the mirror throats and do not extend into the expanders; fluctuations may be artificially truncated by the density floor in Equation 2.1.

Joint time-frequency and azimuthal-mode spectra of density and electric field fluctuations, $\tilde{n}(\omega, m)$ and $\tilde{E}_\theta(\omega, m)$, are presented in Figure 6(a)-(f). Fluctuations are sampled at radii $r = \{3.34, 2.98, 2.69\}\rho_{\mathrm{i}0}$ respectively, over $t = 3$ to $6\,\tau_{\mathrm{bounce}}$; ω is angular frequency. Positive ω/k corresponds to the ion diamagnetic drift direction. We interpret Fourier power at $\omega < 0$ as high-ω signal that is aliased in frequency space and would otherwise be contiguous in physical (ω, k). Assuming so, both $\tilde{n}$ and $\tilde{E}_\theta$ show a mode spectrum with a phase speed $\omega/k > 0$ comparable to the ion diamagnetic drift speed v_{Di} (white dotted lines, Figure 6(a)-(f)). We compute

$$v_{\mathrm{Di}} \approx \frac{T_{\mathrm{i}\perp}/m_{\mathrm{i}}}{\Omega_{\mathrm{i}0}} \left(-\frac{1}{n_{\mathrm{i}}} \frac{\mathrm{d}n_{\mathrm{i}}}{\mathrm{d}r} \right) = v_{\mathrm{ti}0} \frac{T_{\mathrm{i}\perp}}{T_{\mathrm{i}0}} |\epsilon| \rho_{\mathrm{i}0} \tag{3.1}$$

using $\epsilon\rho_{\mathrm{i}0} = \{-1, -1, -1.5\}$ and $T_{\mathrm{i}\perp}$ measured at $t = 6\tau_{\mathrm{bounce}}$ (values reported in §3.1). The spectra align with $\omega/k = v_{\mathrm{Di}}$ within a factor of 2.

A fundamental mode appears at $\omega \in [\Omega_{i0}, 2\Omega_{i0}]$ in all simulations. Fluctuation power extends to $\omega \gtrsim 3\Omega_{i0}$ in all simulations, perhaps up to $\omega \gtrsim 7\Omega_{i0}$ in the $R_m = 64$ simulation, but by eye we do not discern discrete harmonics above $2\Omega_{i0}$. A low-frequency $\omega \ll \Omega_{i0}$ mode with non-zero m appears chiefly in $\tilde{n}$ and weakly in $\tilde{E}_\theta$; we identify this slower motion as fluid interchange and discuss it further in §4.4.

To help interpret Figure 6(a)-(f), we compute the linearly unstable (ω, k) for DCLC in a planar-slab plasma with a spatial density gradient ϵ and uniform background magnetic field ($\nabla B = 0$). In such a plasma, a dispersion relation for exactly-perpendicular electrostatic waves can be obtained by integrating over unperturbed orbits and Taylor expanding f in particle guiding-center coordinate, following[51]. The dispersion relation is then

$$D = 1 + \sum_s \chi_s = 0\,, \tag{3.2}$$

where the perpendicular ($k = k_\perp$) susceptibility of species s reads:

$$\begin{aligned}\chi_s = \left(\frac{\omega_{ps}}{\Omega_s}\right)^2 \Bigg[\left(1 - \frac{\epsilon\omega}{k}\right) \frac{1}{k^2} \sum_{n=-\infty}^{\infty} \frac{n}{\omega - n} \int d^3\mathbf{v} \left(\frac{1}{v_\perp}\frac{\partial f}{\partial v_\perp}\right) J_n^2 \\ - \frac{\epsilon}{k} \sum_{n=-\infty}^{\infty} \frac{1}{\omega - n} \int d^3\mathbf{v} f J_n^2 \Bigg] ,\end{aligned} \tag{3.3}$$

In Equation 3.3, variables are written in a *species-specific* dimensionless form: $\omega/\Omega_s \to \omega$, $k\rho_s \to k$, $\epsilon\rho_s \to \epsilon$, and $v_\perp/v_{ts} \to v_\perp$, where Ω_s is signed (i.e., $\Omega_e < 0$) and $\rho_s \equiv v_{ts}/\Omega_s$. The decision of how to define v_{ts} (with or without $\sqrt{2}$) is given to the user. The plasma frequency $\omega_{ps} = \sqrt{4\pi n_s q_s^2/m_s}$ for each species. The Bessel functions $J_n = J_n(k_\perp v_\perp)$ as usual, with $k_\perp = k$. Equations (3.2)-(3.3) simplify for cold fluid electrons to yield:

$$D = 1 + \chi_i + \frac{\omega_{pe}^2}{\Omega_e^2} + \frac{\omega_{pe}^2}{|\Omega_e|}\frac{\epsilon}{k\omega} = 0 , \tag{3.4}$$

the variables k, ϵ, and ω are now in dimension-ful units. Equation 3.4 is the slab DCLC dispersion relation also used by[36][39], and[40]. In our sign convention, $\epsilon < 0$ obtains DCLC with $\omega/k > 0$ in the ion diamagnetic drift direction. Equation 3.4 also hosts normal modes with $k < 0$ and high phase velocity in the electron diamagnetic drift direction[36], which do not appear in our simulations and so are omitted from our discussion.

The unstable- and normal-mode solutions to Equation 3.4, presented in Figure 6(g)-(l), are computed as follows. First, we take Ω_{i0}, ρ_{i0}, and v_{ti0} as defined in §2.3 to normalize all variables in Equation 3.4. Plasma parameters used for the $R_{\mathrm{m}} = \{20, 41, 64\}$ simulations respectively, are: $\epsilon\rho_{\mathrm{i0}} = \{-1, -1, -1.5\}$; $n_{\mathrm{i}} = \{4, 1.2, 0.5\} \times 10^{12}\ \mathrm{cm}^{-3}$; and $B = \{8.6, 4.1, 2.7\} \times 10^3$ G. Both ϵ and n_{i} describe the plasma edge at the mid-plane $z = 0$ (Figure 5). We take B at $(r, z) = (0, 0)$ to match the variable normalization throughout this manuscript; B at the plasma edge differs by $\lesssim 10\%$. Reduced ion distributions $F(v_\perp) = \int f \,\mathrm{d}v_\parallel$ are measured directly from the plasma edge (Figure 3). Bessel function sums are computed using all terms with index $|n| \leq 40$. The waves and particles at hand have $k_\perp \rho_{\mathrm{i0}} \lesssim 20$ and $v_\perp/v_{\mathrm{ti0}} \lesssim 2$, so the Bessel function argument $(k_\perp \rho_{\mathrm{i0}})(v_\perp/v_{\mathrm{ti0}}) \lesssim 40$. Terms with $n > 40$ contribute little to χ_{i} because the first positive oscillation of $J_n(\xi)$ peaks at $\xi = j'_n > n$, where j'_n is the smallest positive zero of J'_n[59], and $J_n(\xi) \to 0$ quickly as $\xi \to 0$ for $\xi \lesssim n$.

We then compute D on a discrete mesh of $(k, \mathrm{Re}(\omega), \mathrm{Im}(\omega))$; for each k, we identify normal modes (whether stable, damped, or growing) by seeking local minima of D with respect to the complex ω mesh. Our $D \approx 0$ solutions are not exact. To test our solution scheme, we refined our solutions to $D = 0$ by applying a manual root-finder to each (k, ω) normal mode for one set of plasma parameters, and we saw no significant difference.

Figure 6(g)-(i) uses $F(v_\perp)$ measured from the plasma edge at $t = 6\tau_{\text{bounce}} \approx 6\ \mu\text{s}$, showing DCLC modes at marginal instability (more precisely, drift-cyclotron modes since the loss cone is filled).

Figure 6(j)-(l) uses $F(v_\perp)$ measured at $t = 0$ instead to show that initial distributions with empty loss-cones and spatial gradient $\epsilon\rho_{\text{i0}} \sim \mathcal{O}(1)$ drive strongly unstable, broad-band electrostatic modes with fastest growth towards high $k\rho_{\text{i0}} \gg 1$ and $\omega \gg \Omega_{\text{i0}}$. The $R_{\text{m}} = 64$ simulation (Figure 6(l)) is an exception, because its CQL3D-m model predicts a larger population of trapped cool ions that helps stabilize DCLC. Figure 6(l) also reveals three branches of unstable modes, each with distinct ω/k, that we speculate may be drift waves associated with distinct hot and cool plasma populations (Figure 3(a), (d)). The slowest branch is visible with $\text{Re}(\omega)$ between 2 to $4\Omega_{\text{i0}}$; the corresponding $\text{Im}(\omega)$ are plotted in green. The faster phase speed branches have unstable $\text{Re}(\omega) > 4\Omega_{\text{i0}}$ extending to at least $14\Omega_{\text{i0}}$; the corresponding $\text{Im}(\omega)$ are plotted in light red.

What is learned from comparing the simulation spectra versus linear theory in Figure 6? First, marginally-stable DCLC mode growth may explain high $k\rho_{\text{i0}} \gtrsim 5$ fluctuations residing in the device during steady-state decay. How do we explain the fundamental mode between $\omega = \Omega_{\text{i0}}$ and $2\Omega_{\text{i0}}$ for simulations with $R_{\text{m}} = 41, 64$, since that mode is predicted to be linearly stable at late times? It may be an initially excited mode that did not damp and so persists to late times; this appears possible for the $R_{\text{m}} = 41$ simulation, where the fundamental is unstable at $t = 0$. Or, it may be excited by non-linear flow of wave energy from unstable to stable modes; such an explanation may be needed for the $R_{\text{m}} = 64$ simulation, in which cool plasma at the radial edge should quench DCLC growth of the fundamental mode at both $t = 0$ and $t = 6\ \mu\text{s}$. We have interpreted the $t = 0$ and $t = 6\ \mu\text{s}$ as most- and least-unstable scenarios for DCLC growth, but the plasma may also transition through other states that destabilize the fundamental mode.

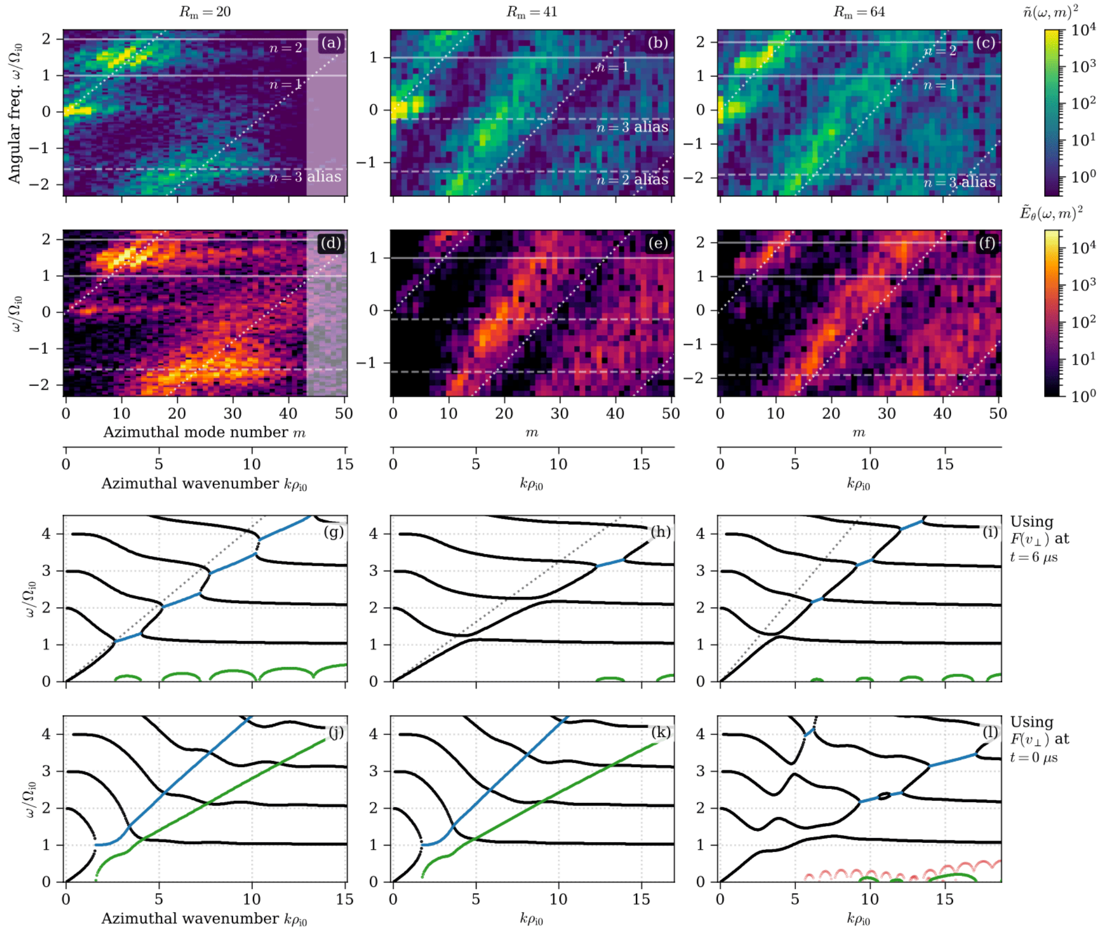

Figure 6. Time-azimuth Fourier spectra of density $\tilde{n}(\omega, m)^2$ (panels (a)-(c)) and electric field $\tilde{E}_\theta(\omega, m)^2$ (panels (d)-(f)) for simulations with $R_\text{m} = \{20, 41, 64\}$ (left to right). Bottom rows show corresponding (ω, k) of unstable DCLC modes predicted by Equation 3.4 for edge $F(v_\perp)$ at $t \approx 6\mu$s (panels (g)-(i)) or $t = 0$ (panels(j)-(l)). In panels (a)-(f), the full ω range within Nyquist-sampling limits is shown; signals with $\omega \gtrsim 2\Omega_\text{i0}$ alias in frequency. White dotted lines plot ion diamagnetic drift velocity $\omega/k = v_\text{Di}$. Shaded vertical bar in (a),(d) marks grid resolution limit $k > \pi/\Delta r$ with $\Delta r = \sqrt{2}\Delta x$. In panels (g)-(l), we plot both stable- and unstable-mode frequencies $\text{Re}(\omega)$ (black, blue), and also the corresponding unstable-mode growth rates $\text{Im}(\omega)$ (green). In panel (l) only, red curves plot $\text{Im}(\omega)$ for higher-ω/k modes with $\text{Re}(\omega) \in [4\Omega_\text{i0}, 14\Omega_\text{i0}]$ beyond the plot extent. Black dotted lines plot $\omega/k = v_\text{Di}$.

3.3. Ion Scattering

To establish a causal link between δE fluctuations and axial ion losses, we quantify ion scattering in the $R_\text{m} = 20$ simulation as follows. We measure velocity jumps over a short time interval $\delta t \equiv t_1 - t_0 = 0.25\Omega_\text{i0}^{-1}$ for $\mathcal{O}(10^7)$ PIC macro-particles sampled from $|z| \in [0, 5.9]$ cm. Our approach is similar to *many* other PIC simulation studies; see[60] for a recent discussion of nuances in constructing and interpreting such velocity jump moments. Figure 7(a) shows the probability distribution of the $\mathbf{B}$-perpendicular and parallel velocity jumps, $\delta v_\perp = v_\perp(t_1) - v_\perp(t_0)$ and $\delta v_\parallel = v_\parallel(t_1) - v_\parallel(t_0)$. The distributions are not Gaussian and have long tails. The perpendicular jumps $\delta v_\perp$ are much larger than $\delta v_\parallel$, as expected for flute-like ($k_\perp \gg k_\parallel$) electrostatic modes and as evident in Figure 3.

Ion velocities may jump due to both adiabatic and non-adiabatic motion. To separate these motions, introduce an energy $\mathcal{E} = m_\mathrm{i} v^2/2 + e\langle\phi\rangle_{\theta,t}$, where $\langle\cdots\rangle_{\theta,t}$ is an average over both azimuth angle θ and time from t_0 to t_1. We expect $\mathcal{E}$ to be conserved by particles gyrating in slowly-varying $\mathbf{E}$ and $\mathbf{B}$ fields, at lowest order in a Larmor-radius expansion. Therefore, we attribute jumps in $\mathcal{E}$ to a non-adiabatic kick in perpendicular velocity that we call $\delta v_{\perp\mathcal{E}}$. We use $\delta\mathcal{E} = \mathcal{E}(t_1) - \mathcal{E}(t_0) = m v_\perp \delta v_{\perp\mathcal{E}} - m(\delta v_{\perp\mathcal{E}})^2/2$ to compute:

$$\frac{\delta v_{\perp\mathcal{E}}}{v_\perp(t_1)} = 1 - \sqrt{1 - \frac{2\delta\mathcal{E}}{m v_\perp^2(t_1)}}\,. \tag{3.5}$$

Equation 3.5 requires $\delta\mathcal{E}$ to not exceed the particle's final perpendicular energy:

$$\delta\mathcal{E} < m v_\perp^2(t_1)/2\,. \tag{3.6}$$

Figure 7(a) shows that the probability distribution of $\delta v_{\perp\mathcal{E}}$, computed only for those particles satisfying Equation 3.6, is marginally narrower than that of $\delta v_\perp$, as expected if non-adiabatic kicks are the main contribution to $\delta v_\perp$.^{5}

The ion diffusion $\langle \delta v_{\perp\mathcal{E}} \delta v_{\perp\mathcal{E}} \rangle/\delta t$ as a function of radius is shown in Figure 7(b); its value is normalized to $v_{\mathrm{A}0}^2 \Omega_{\mathrm{i}0}$ in all of Figure 7(b)-(g), where $v_{\mathrm{A}0} = B/\sqrt{4\pi n m_\mathrm{i}}$ with $n = 3 \times 10^{13}\ \mathrm{cm}^{-3}$ is a reference Alfvén velocity. Here, $\langle\cdots\rangle$ is a velocity-distribution moment computed in radial bins. The use of $\delta v_{\perp\mathcal{E}}$ decreases the measured diffusion as compared to $\langle \delta v_\perp \delta v_\perp \rangle/\delta t$, as expected.

The ion diffusion due to fluctuating fields $\delta E_\perp(\boldsymbol{r})$ can be described by a diffusion coefficient similar to those used in quasi-linear models:

$$D_{\perp\perp} = \frac{1}{2}\left(\frac{e}{m_\mathrm{i}}\delta E_\perp\right)^2 \tau_\mathrm{c}\,, \tag{3.7}$$

where τ_c is a yet-unknown wave-particle correlation time. Equation 3.7 assumes (i) weak but *coherent* kicks $\delta v_\perp \approx (e/m_\mathrm{i})\delta E_\perp \tau_\mathrm{c}$; (ii) a uniform random distribution of angles between $\boldsymbol{v}_\perp$ and $\delta\boldsymbol{E}_\perp$ to obtain a factor of $1/2$ accounting for kicks in gyrophase instead of $v_\perp$ magnitude. For a scattering-measurement time $\delta t < \tau_\mathrm{c}$, we expect

$$D_{\perp\perp} \approx \frac{\langle \delta v_{\perp\mathcal{E}}\, \delta v_{\perp\mathcal{E}} \rangle}{\delta t} \,, \tag{3.8}$$

also replacing $\tau_\mathrm{c} \to \delta t$ in $D_{\perp\perp}$.

Choosing $\delta t < \tau_c$ is unusual for studies of particle diffusion, as the resulting Equation 3.8 describes a more "ballistic" than diffusive process. But, a short δt helps us. When using a longer $\delta t \gg \tau_c$, at least two issues arise. First, ions gyrate in and out of the scattering zone, as the zone's radial width is similar to an ion Larmor radius. A typical ion may get one or a few kicks, gyrate out of the scattering zone and drift adiabatically, re-enter the scattering zone to be kicked again, and so on, resulting in a random walk with intermittent large time gaps. The scattering zone's finite radial width may also introduce bias in the correlation time τ_c, because a typical inboard (small r) ion gyrating in and out of the scattering zone sees a redshift $\omega - k_\perp v_\perp$, whereas a typical outboard (large r) ion instead sees a blueshift $\omega + k_\perp v_\perp$. Second, a longer δt needed to sample multiple gyration periods $2\pi\Omega_{i0}^{-1}$ will introduce axial bounce effects. In the $R_m = 20$ simulation, $\tau_\mathrm{bounce} \approx 40\Omega_{i0}^{-1}$, and even fewer ion gyrations are executed within τ_bounce for the higher R_m cases.

In Figure 7(c) we compare Equation 3.8 to the ion diffusion measured from individual particles. The fluctuating energy density is azimuth averaged as $\delta E_r^2 = \langle E_r^2 \rangle_\theta - {\langle E_r \rangle_\theta}^2$, and similarly for δE_θ^2; the sum $\delta E_\perp^2 = \delta E_\theta^2 + \delta E_r^2$. The diffusion due to δE_θ^2 agrees especially well with the particle measurement, whereas the diffusion due to δE_r^2 agrees less well.

Numerical noise might drive axial losses from the plasma edge in the same way that we are attributing to DCLC, because PIC particle count decreases at the plasma edge. To check this possibility, Figure 7(d) shows that the measured ion scattering is converged in the number of particles per cell used. We are confident that ion scattering is not due to numerical noise because (i) the DCLC electric fields have much larger energy density than numerical noise at the grid scale, and Figure 7(c) shows good agreement in radial profiles of electric fields and scattering, (ii) we see weak to no N_ppc dependence of scattering rates, whereas if scattering were due to noise, we might expect either an outwards shift in r as N_ppc increases (for fixed DCLC amplitude), or a decrease in scattering rate if noise suppresses DCLC amplitude; (iii) ion scattering is clearly anisotropic (Figure 7(a)), whereas numerical scattering should be insensitive to $v_\parallel$ versus $v_\perp$ because the grid scale is much smaller than the ion Larmor radius.

In Figure 7(e) we show the effect of δt upon the radial profiles of measured ion diffusion. Figure 7(f) then samples the ion scattering at its radial peak $r = 8.2\ \mathrm{cm}$ (blue curve) and shows its dependence upon many more values of δt. We see that the diffusion moment scales linearly with small δt as expected from Equation 3.8; for comparison, the black dotted line shows an exactly linear correlation with δt. As δt becomes $\gtrsim \Omega_{i0}^{-1}$, waves and particles decorrelate and the diffusion rate begins to fall. We perform a similar calculation at $(r, z) \approx (6.8, 50)\ \mathrm{cm}$ (Figure 7(f), orange curve) to conclude that τ_c is shorter near the fast ion turning point. If $\tau_c \sim 1/\Omega_i$ (where Ω_i varies with z, unlike Ω_{i0}), the lower τ_c can be easily explained by the $2\times$ increase in B magnitude.

Finally, Figure 7(g) shows $\langle \delta v_{\perp\mathcal{E}} \delta v_{\perp\mathcal{E}} \rangle / \delta t$ as a function of (r, z) in the mirror's central cell. The ion scattering at all z is well localized to the same flux surfaces between beam-ion turning points. Scattering is strongest towards $z = 0$, where the central-cell field is relatively uniform.

We conclude from Figure 7(e)-(f) that particle scattering has longer correlation time τ_{c} and reaches larger amplitude at the mirror mid-plane $z = 0$, as compared to near the beam-ion turning points. Ions at $z = 0$, and throughout the central cell where $B \approx B(z = 0)$, should be more important for regulating DCLC growth and saturation than ions at the turning points.

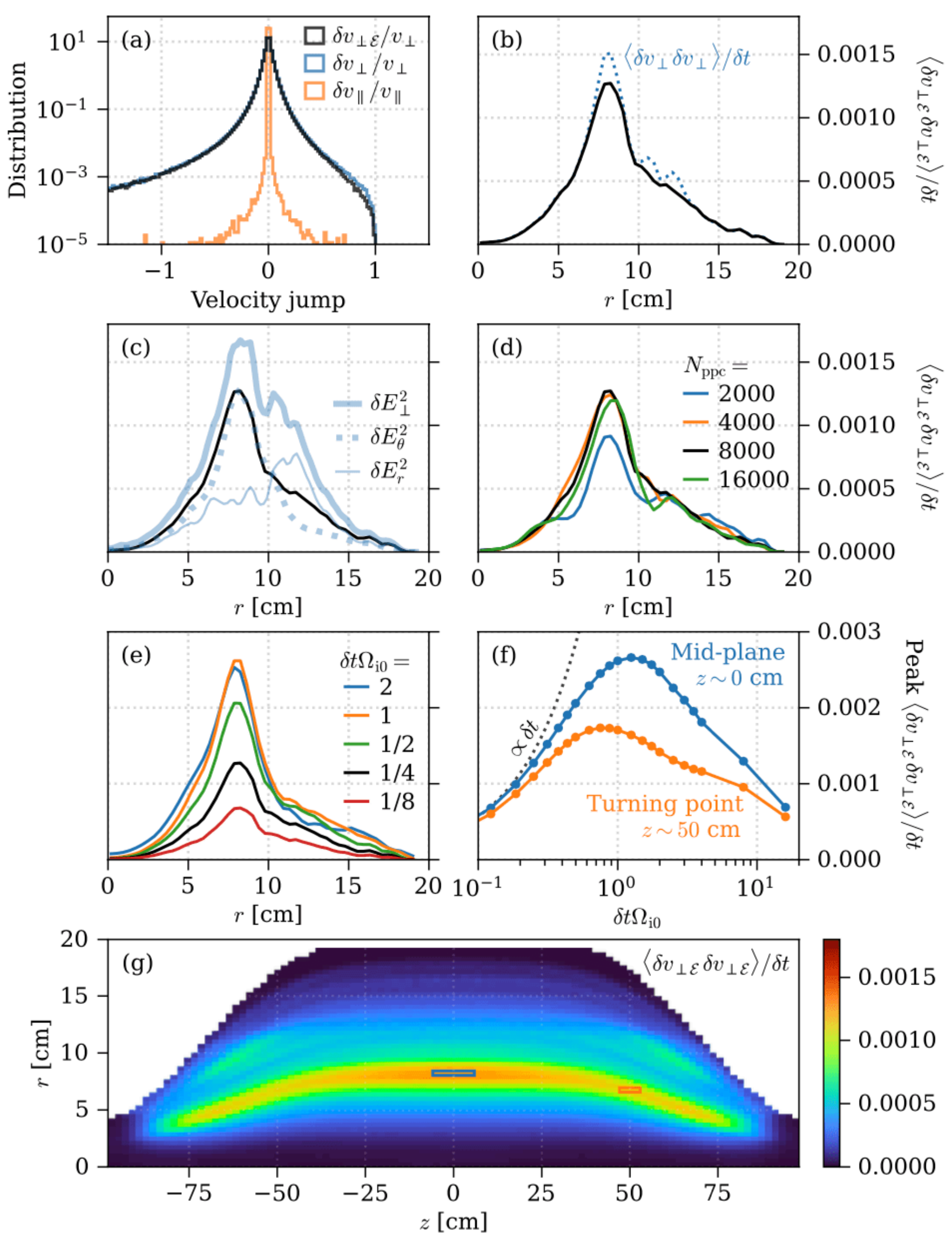

Figure 7. Ion scattering measurements in $R_\text{m} = 20$ simulation, at mid-plane $z \in [-5.9, 5.9]$ cm unless said otherwise. (a): Probability distribution of ion velocity jumps, normalized to $v_\perp(t_1)$ and $v_\parallel(t_1)$, for particles at all radii. (b): Radial profile of ion diffusion $\langle\delta v_{\perp\mathcal{E}}\delta v_{\perp\mathcal{E}}\rangle/\delta t$ (solid black) compared to $\langle\delta v_\perp\delta v_\perp\rangle/\delta t$ (dotted blue). (c): Predicted radial profile of ion diffusion due to fluctuating fields δE_θ^2 (dotted blue), δE_r^2 (thin solid blue), and $\delta E_\perp^2 = \delta E_\theta^2 + \delta E_r^2$ (thick solid blue), compared to $\langle\delta v_{\perp\mathcal{E}}\delta v_{\perp\mathcal{E}}\rangle/\delta t$ (solid black). (d): Numerical convergence in particles per cell for radial profile of $\langle\delta v_{\perp\mathcal{E}}\delta v_{\perp\mathcal{E}}\rangle/\delta t$. (e): Effect of scattering

measurement time δt upon radial profile of $\langle \delta v_{\perp \mathcal{E}} \delta v_{\perp \mathcal{E}} \rangle / \delta t$. (f): Effect of scattering measurement time δt upon diffusion measured at the mid-plane $(r, z) \approx (8.2, 0)$ cm (blue curve), and near the beam-ion turning point at $(r, z) \approx (6.8, 50)$ cm (orange curve). (g) 2D map of diffusion $\langle \delta v_{\perp \mathcal{E}} \delta v_{\perp \mathcal{E}} \rangle / \delta t$ computed in discrete (r, z) bins (pixels); only bins with > 100 particles are shown. Light blue and orange boxes mark measurement locations used in panel (f). In panels (b)-(g), all values of $\langle \delta v_{\perp \mathcal{E}} \delta v_{\perp \mathcal{E}} \rangle / \delta t$ are normalized to $v_{\mathrm{A0}}^2 \Omega_{\mathrm{i0}}$.

3.4. Particle Confinement Time

Because the loss cone is full—i.e., $F(v_\perp)$ is roughly constant within the loss cone (Figure 3)—our simulated mirrors are a collisionless analog of the Gas Dynamic Trap (GDT) at the Budker Institute[61]. Ions scatter across the loss-cone boundary as fast as (or faster than) untrapped ions can stream out of the mirror, implying an effective mean free path shorter than the device's length. The particle confinement time $\tau_{\mathrm{p}} \equiv N / (\mathrm{d}N/\mathrm{d}t)$, where N is the total number of ions, then scales like the eponymous "gas dynamic" time:

$$\tau_{\mathrm{GD}} = \frac{2 L_{\mathrm{p}} R_{\mathrm{m}}}{v_{\mathrm{ti}\parallel}}, \tag{3.9}$$

adapted from[1] with $v_{\mathrm{ti}\parallel}$ a characteristic parallel thermal velocity.

To test the relation $\tau_p \propto \tau_{\mathrm{GD}}$, we measure τ_p between $t = 5$ to $6\,\tau_{\mathrm{bounce}}$, and $v_{\mathrm{ti}\parallel} = \langle v_\parallel^2 \rangle^{1/2}$ at $t = 6\,\tau_{\mathrm{bounce}}$, in each of the $R_{\mathrm{m}} = \{20, 41, 64\}$ simulations with $L_{\mathrm{p}} = 98$ cm on axis. We also measure τ_p and $v_{\mathrm{ti}\parallel}$ in additional $R_{\mathrm{m}} = 20$ simulations with varying $T_{\mathrm{e}} = 0, 2.5, 5, 10$ keV and longer central cells (larger L_{p}); the latter are constructed as follows. Split the "original" mirror device in half at $z = 0$. Between the mirror halves, insert a cylindrical plasma of length 98 or 168 cm, thereby increasing the entire mirror's half-length L_{p} by 1.5 or $2\times$. The cylinder has, at all z, the same velocity distribution and magnetic field $\mathbf{B}$ as in the original mirror at $z = 0$. The simulation domain is made larger; mesh voxel dimensions (Δx, Δy, Δz) are the same as in §2. The cylinder's magnetic field is unphysical because it has $\mathrm{d}B_z/\mathrm{d}r \neq 0$ and $B_r = 0$, implying non-zero current $c \nabla \times \mathbf{B} / (4\pi)$, so we exclude this current from the $\mathbf{j} \times \mathbf{B}$ term in Ohm's Law (Equation 2.1).

The confinement time $\tau_p \sim \mathcal{O}(10^2)$ μs, and τ_p scales linearly with τ_{GD} as expected (Figure 8(a)). Gas-dynamic confinement explains losses from the $R_{\mathrm{m}} = 20$ and 41 simulations very well. Raising electron temperature T_{e} from 0 to 10 keV lowers τ_p from 57 to 35 μs for the $R_{\mathrm{m}} = 20$ simulations. The $R_{\mathrm{m}} = 64$ shows 20% better particle confinement than predicted by Equation 3.9. Why? The larger plasma radius and hence longer flux-tube length $> 2L_\mathrm{p}$ between mirror throats only explains $\sim 5\%$ of the disagreement. We speculate that electrostatic potential effects may explain the remaining disagreement. In the $R_\mathrm{m} = 20, 41$ cases, beam ions diffuse in $v_\perp$ and escape with high $v_\parallel$; electrostatic effects are weak since $T_\mathrm{e} \ll T_\mathrm{i}$, so Equation 3.9 accurately describes the beam ion confinement. The $R_\mathrm{m} = 64$ case has more cool, low-temperature ions (Figure 3(i)) that can be trapped by the sloshing-ions' potential peak at $z \sim 30$ cm, also called a Yushmanov potential; confinement is thus improved.

Instabilities in many settings are self regulating; i.e., unstable waves drive phase-space flow that quenches the waves' own energy source, driving the system to equilibrium[62]. If DCLC self regulates, then we may expect its amplitude to grow in time until the diffusion rate into the loss cone balances the axial outflow rate: $\nu_{\perp\perp} \propto \tau_\mathrm{GD}^{-1}$. We test this by computing a diffusion rate into the loss cone as:

$$\nu_{\perp\perp} \equiv \frac{1}{N_\ell} \int \frac{D_{\perp\perp}(r)}{{v_{\perp\mathrm{LC}}}^2} n_\mathrm{i}(r) 2\pi r \ell \, \mathrm{d}r \,, \tag{3.10}$$

which is a density-weighted average of $D_{\perp\perp}$ (Equation 3.7) over a cylindrical kernel of axial length ℓ and radial profile $n_\mathrm{i}(r)$, normalized to $N_\ell = \int n_\mathrm{i}(r) 2\pi r \ell \mathrm{d}r$. We take $v_{\perp\mathrm{LC}} = v_{\mathrm{ti}\parallel}/\sqrt{R_\mathrm{m} - 1}$ to approximate the ions' $v_\perp$ at the loss cone boundary, we take $\ell = 12$ cm centered at $z = 0$, and we take $\tau_\mathrm{c} = \Omega_\mathrm{i0}^{-1}$. Given these assumptions, and given that Equation 3.7 is not from a self-consistent quasi-linear theory, we interpret Equation 3.10 as no more accurate than an order-of-magnitude scaling. In Figure 8(b) we compute the diffusion timescale $1/\nu_{\perp\perp}$ using either δE_θ^2 or $\delta E_\perp^2$ as defined as in Figure 7(c). We observe that $1/\nu_{\perp\perp}$ has similar magnitude as τ_GD, as expected. But, no trend is obvious from the scatter and few data points.

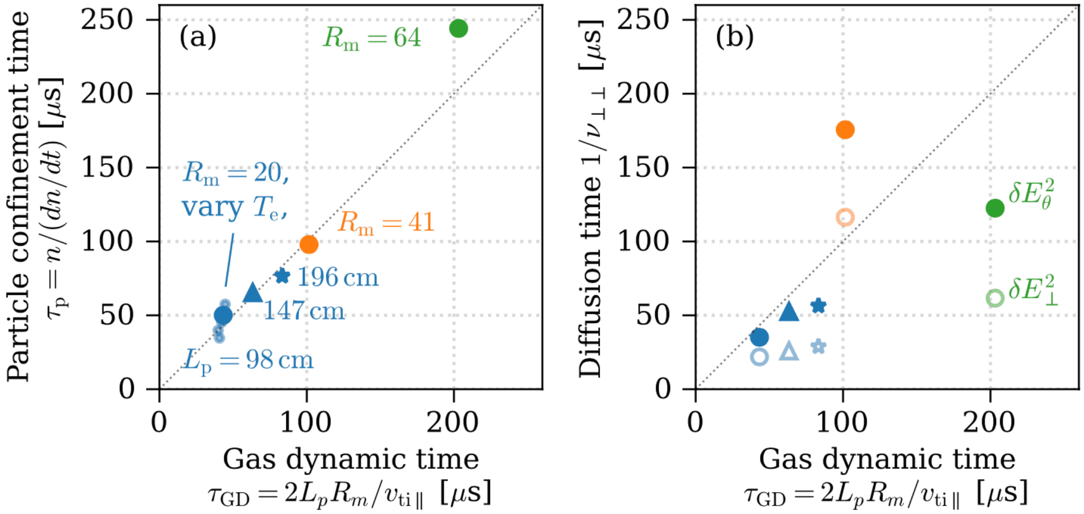

Figure 8. (a): Particle confinement time measured between $t = 5$ to $6\tau_\mathrm{bounce}$, for mirrors of varying R_m (blue, orange, green) and device length L_p (circle, triangle, star markers) as a function of τ_GD (Equation 3.9). Small blue markers vary T_e for $R_\mathrm{m} = 20$; large blue marker is fiducial $T_\mathrm{e} = 1.25$ keV. (b): Diffusion timescale $1/\nu_{\perp\perp}$ (Equation 3.10) modeled from δE_θ^2 (solid markers) and $\delta E_\perp^2$ (hollow markers), as a function of τ_GD. In both panels, dotted black line is $\tau_\mathrm{p} = \tau_\mathrm{GD}$.

4. Discussion

4.1. Cool Plasma Effects

How much cool plasma, and at what temperature, suppresses DCLC for the peaked beam-ion distributions injected into WHAM? To answer this, Figure 9 computes DCLC linear stability with distinct "hot" and "cool" ion populations. The hot ions are a beam distribution at $t = 0$ in our $R_\mathrm{m} = 20$ simulation, taken from the mid-plane $z = 0$ (Figure 3(b)), with $n_\mathrm{hot} = 4 \times 10^{12}$ cm^{-3}. The cool ions are a Maxwellian of the same species (deuterium), with density n_cool and temperature T_cool. We solve Equation 3.4 using the same procedure as in §3.2, within a finite domain $k\rho_\mathrm{i0} < 15$, $\mathrm{Re}(\omega)/\Omega_\mathrm{i0} < 10$, and $\mathrm{Im}(\omega)/\Omega_\mathrm{i0} < 4$.

Figure 9(a) predicts that DCLC is suppressed when cool and hot ion densities are nearly equal, and $T_\mathrm{cool} \sim 2$ to 10 keV. In cases where DCLC is not fully stabilized, panel (b) shows that dense-enough cold plasma will at least stabilize low harmonics (compare Figure 9(g)), pushing the unstable DCLC modes towards higher harmonics of Ω_i0, which should weaken DCLC's scattering rate. The Figure 9(b) prediction qualitatively concurs with recent measurements on the GDT device: DCLC at high harmonics was observed when a relatively high gas density is puffed into GDT's central chamber before neutral-beam injection[21][22]; critically, this form of DCLC did not impede build-up of plasma pressure. Panels (c)-(h) show the effect of varying T_{cool} (with $n_{\mathrm{cool}} = n_{\mathrm{hot}}$) on the corresponding DCLC modes. As T_{cool} rises, quenching of low harmonics proceeds to total stabilization. When T_{cool} is close to the beam ions' effective temperature, the "cool" plasma is less able to reduce the velocity-space gradient $\mathrm{d}F/\mathrm{d}v_{\perp}$, and DCLC become unstable at all ion-cyclotron harmonics.

To test the predictions of Figure 9, we repeat the $R_{\mathrm{m}} = 20$ Hybrid-VPIC simulation with varying amounts of cool plasma added to the radial edge: $n_{\mathrm{cool}} \approx \{4, 8, 16\} \times 10^{12}\ \mathrm{cm}^{-3}$ within radii $r \sim 5$ to $12\ \mathrm{cm}$ (Figure 10(a)), with $T_{\mathrm{cool}} = 1\ \mathrm{keV}$. The cool plasma quenches DCLC losses and improves the hot-plasma confinement by a factor of $\sim$2 to 5× (Figure 10(b)). The simulation with lowest $n_{\mathrm{cool}} = 4 \times 10^{12}\ \mathrm{cm}^{-3}$ shows that cool ions are better confined than the hot ions, qualitatively consistent with trapping by the sloshing ions' axial potential and lower outflow speed $v_{\mathrm{ti}\parallel}$ in Equation 3.9. At higher n_{cool}, the cool-ion confinement degrades, which may be due to flattening of ion density n, and hence also electric potential ϕ, along z.

Comparing Figures 9 and 10, we see some discrepancy. The Hybrid-VPIC simulations quench DCLC losses at higher $n_{\mathrm{cool}}/n_{\mathrm{hot}}$ than predicted by the linear theory. We also performed simulations with varying $T_{\mathrm{cool}} = \{1, 2, 5\}\ \mathrm{keV}$; the hot-ion confinement is poorer with $T_{\mathrm{cool}} = 5\ \mathrm{keV}$ as compared to lower T_{cool}, which also contrasts with the linear-theory prediction that $T_{\mathrm{cool}} = 5\,\mathrm{keV}$ with $n_{\mathrm{cool}}/n_{\mathrm{hot}} \sim 1$ fully stabilizes DCLC within the $(k, \mathrm{Re}(\omega), \mathrm{Im}(\omega))$ domain used in Figure 9, and so should be more stabilizing than $T_{\mathrm{cool}} = 1\,\mathrm{keV}$. But, we emphasize that for all values of T_{cool} considered, with $n_{\mathrm{cool}} \geq 8 \times 10^{12}\ \mathrm{cm}^{-3}$, the hot-ion confinement is better than in the fiducial simulation without any cool plasma.

The aforementioned discrepancy between Figures 9 and 10 may be explained by some combination of (i) weaker electrostatic trapping and faster outflow $v_{\mathrm{ti}\parallel}$ as T_{cool} increases, and (ii) quasi-linear diffusion of beam ions towards the loss cone, which shifts the unstable drive $\mathrm{d}F/\mathrm{d}v_{\perp}$ to lower $v_{\perp}$ so that lower T_{cool} becomes stabilizing. Let us expand on point (ii). For a quasi-linearly diffused $F(v_{\perp})$, the relevant T_{cool} is set not by the injected beam distribution, but instead by the loss-cone's $v_{\perp}$ boundary value *at the injected beam's characteristic* $v_{\parallel}$. For WHAM's 45° pitch-angle beam, DCLC-scattered ions escape at the loss-cone boundary value $v_{\perp} \sim \sqrt{2E_{\mathrm{beam}} \cos^2\theta_{\mathrm{NBI}}/m_{\mathrm{i}}/(R_{\mathrm{m}} - 1)}$, which corresponds to perpendicular energy $m_{\mathrm{i}} v_{\perp}^2/2 \sim 0.7\ \mathrm{keV}$ for primary beam energy $E_{\mathrm{beam}} = 25\ \mathrm{keV}$,

$\theta_{\mathrm{NBI}} = 45^\circ$, and $R_{\mathrm{m}} = 20$. For 2XIIB and other mirrors with 90° pitch-angle beams, the loss cone boundary at $v_\parallel \sim 0$ is instead set by the axial electric potential, $v_\perp \sim \sqrt{2q_{\mathrm{i}}\Delta\phi/m_{\mathrm{i}}/(R_{\mathrm{m}}-1)}$[6] where $\Delta\phi$ is the axial potential drop from mid-plane to throat. We conclude that $T_{\mathrm{cool}} \sim 1$ keV can quench DCLC with marginally-stable ion distributions in WHAM, which helps reconcile Figures 9 and 10. We further observe that there is no conflict between 2XIIB's empirical stabilization of DCLC with $T_{\mathrm{cool}} \sim 100$ eV streaming plasma[63] and our work showing that WHAM may stabilize DCLC with $T_{\mathrm{cool}} \sim 1$ keV plasma; the appropriate T_{cool} for each device is mediated by the beam injection angle.

Cool ions also drive faster growing MHD interchange-like modes in our Hybrid-VPIC simulations; if our simulations were run longer than $t = 6$ μs, these interchanges might eventually cause large ion losses. In laboratory devices, interchange motions can be stabilized by shear flow; such flows can be driven by either external voltage biasing[64][65] or electron cyclotron heating[66]. We thus remain optimistic that cold plasma stabilization can work in WHAM, especially given the method's success in real laboratory experiments[11][22].

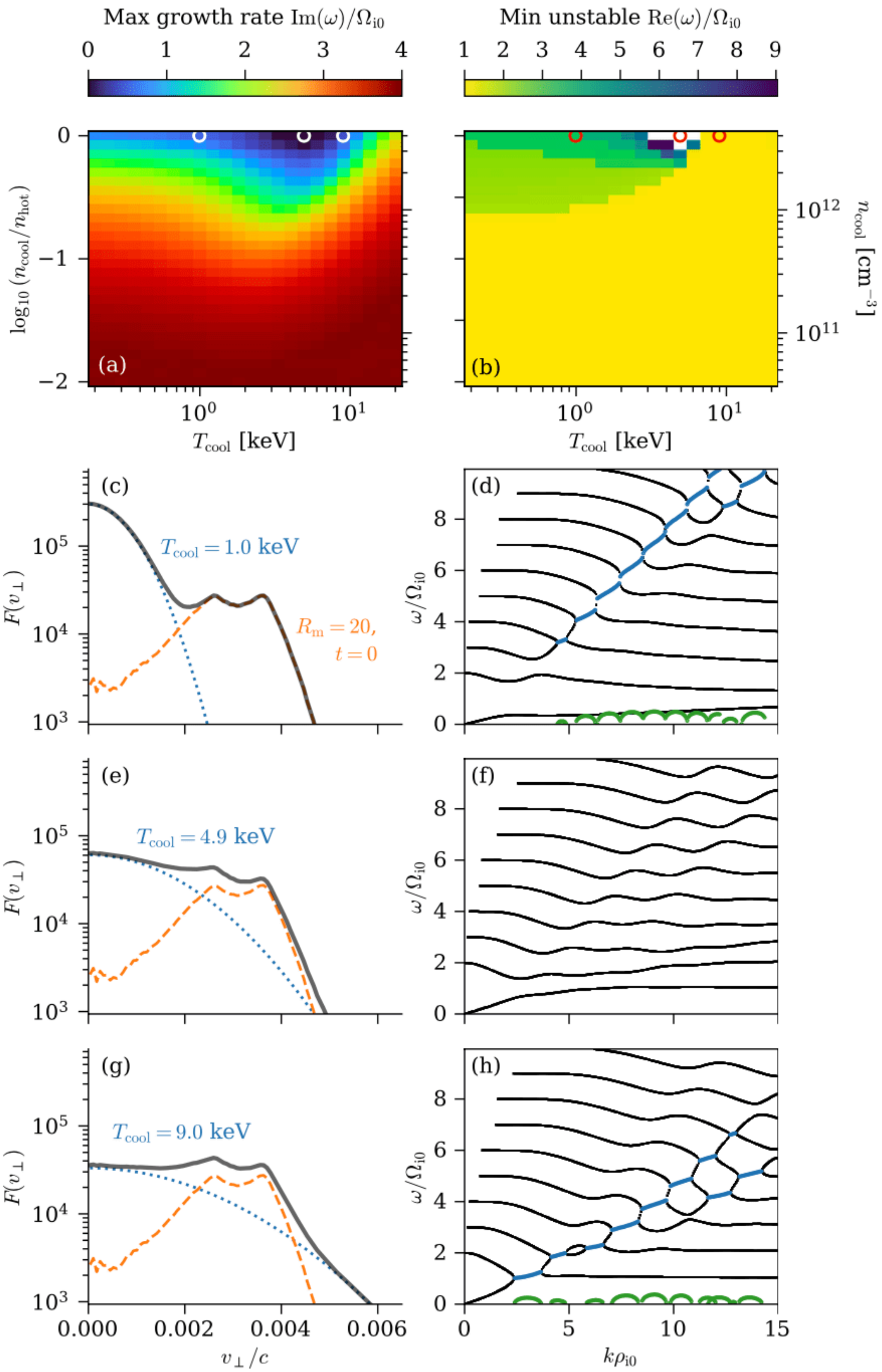
Max growth rate $\mathrm{Im}(\omega)/\Omega_{\mathrm{i0}}$
0
1
2
3
4
Min unstable $\mathrm{Re}(\omega)/\Omega_{\mathrm{i0}}$
1
2
3
4
5
6
7
8
9
$\log_{10}(n_{\mathrm{cool}}/n_{\mathrm{hot}})$
0
-1
-2
(a)
10^0
10^1
T_{cool} [keV]
(b)
10^0
10^1
T_{cool} [keV]
10^{12}
10^{11}
n_{cool} [cm^{-3}]
(c)
$F(v_\perp)$
10^5
10^4
10^3
$T_{\mathrm{cool}} = 1.0$ keV
$R_{\mathrm{m}} = 20,$
$t = 0$
(d)
$\omega/\Omega_{\mathrm{i0}}$
8
6
4
2
0
(e)
$F(v_\perp)$
10^5
10^4
10^3
$T_{\mathrm{cool}} = 4.9$ keV
(f)
$\omega/\Omega_{\mathrm{i0}}$
8
6
4
2
0
(g)
$F(v_\perp)$
10^5
10^4
10^3
$T_{\mathrm{cool}} = 9.0$ keV
0.000
0.002
0.004
0.006
$v_\perp/c$
(h)
$\omega/\Omega_{\mathrm{i0}}$
8
6
4
2
0
0
5
10
15
$k\rho_{\mathrm{i0}}$

Figure 9. Effect of cool plasma on DCLC linear stability in WHAM with $R_\mathrm{m} = 20$ and a hot beam-ion distribution. (a): 2D regime map of maximum growth rate $\mathrm{Im}(\omega)/\Omega_{\mathrm{i}0}$ as a function of n_cool and T_cool. (b): Like (a), but showing minimum $\mathrm{Re}(\omega)/\Omega_{\mathrm{i}0}$ that is DCLC unstable. As cool plasma density is raised, low harmonics are stabilized. White pixels at top of panel ($T_\mathrm{cool} \sim 5$ keV and $\log_{10}(n_\mathrm{cool}/n_\mathrm{hot}) \sim 0$) mean that no linearly-unstable modes were found. (c): Example ion distribution $F(v_\perp)$ with 1 keV cool plasma (dotted blue) added to initial $R_\mathrm{m} = 20$ distribution. (d): Dispersion relation solutions corresponding to (c), showing normal modes (black), unstable mode $\mathrm{Re}(\omega)$ (blue), and unstable mode $\mathrm{Im}(\omega)$ (green). (e-f): like (c-d), but with 4.9 keV cool plasma. (g-h): like (c-d), but with 9.0 keV cool plasma.

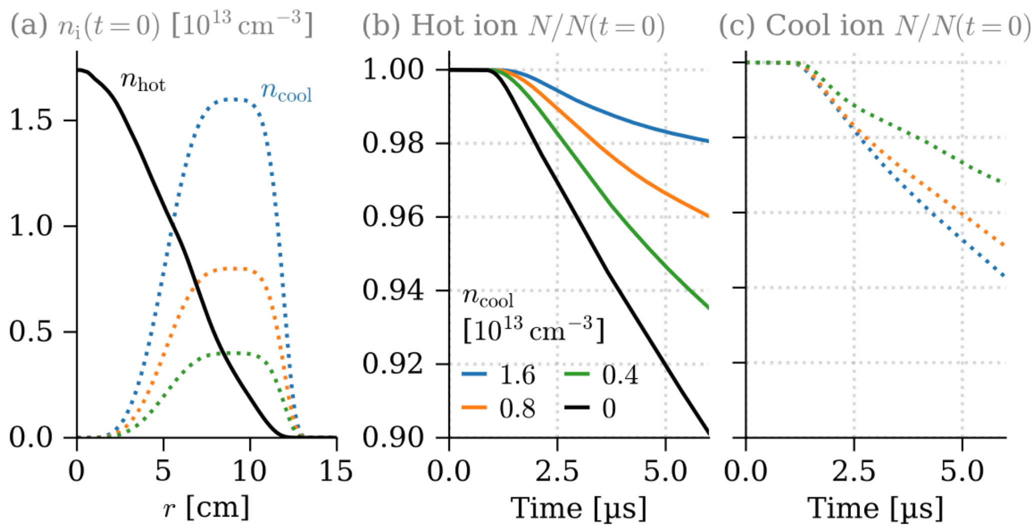

Figure 10. Effect of cool (1 keV) plasma on particle losses in Hybrid-VPIC simulations with $R_\mathrm{m} = 20$. (a) Initial density radial profiles for hot ions (black solid curve) and cool ions (colored dotted curve), (b) Total number of hot ions within simulation domain, normalized to initial value, for simulations with varying n_cool. (c) Like panel (b), but showing the total number of cool ions.

4.2. *Spatial Gradient Effects*

A smaller spatial gradient $\epsilon\rho_{\mathrm{i}0}$ also helps to stabilize DCLC[6][15][24]. Figure 11 shows this for plasma parameters similar to the physically-larger, Break-Even Axisymmetric Mirror (*BEAM*) design concept of[4]. We re-compute DCLC linear stability for *BEAM*'s radial edge comprising (i) hot deuterium/tritium (D/T) beam ions, with equal densities of D/T and temperature $T \approx 60$ keV[4], and (ii) cool Maxwellian ions with varying n_{cool}, T_{cool}, and isotope choice of hydrogen, deuterium, tritium, or a D/T mixture (equal densities of D/T). The stability calculation assumes $\epsilon\rho_{\mathrm{i0}} = -0.04$, $B = 3$ T, and $n_{\mathrm{hot}} = 6 \times 10^{13}$ cm^{-3} counting both D/T species. The value $1/|\epsilon\rho_{\mathrm{i0}}| = 25$ approximately matches the DCLC design constraint $a/\rho_{\mathrm{i}} = 25$ used by both[4][55]. For normalization, we take $\rho_{\mathrm{i0}} = 1.2$ cm and $f_{\mathrm{ci0}} = 22.9$ MHz. We solve Equation 3.4 using the same procedure as in §3.2, within a finite domain $k\rho_{\mathrm{i0}} < 30$, $\mathrm{Re}(\omega)/\Omega_{\mathrm{i0}} < 10$, and $\mathrm{Im}(\omega)/\Omega_{\mathrm{i0}} < 5$. The domain is larger than before because DCLC appears at larger $k\rho_{\mathrm{i0}}$; the relevant k may be estimated for the n-th cyclotron harmonic as $k\rho_{\mathrm{i0}} \approx n/(|\epsilon|\rho_{\mathrm{i0}})/(T_{\mathrm{i}\perp}/T_{\mathrm{i0}})$, from requiring that the ion diamagnetic drift $\omega/k = v_{\mathrm{Di}}$ intersects the harmonics $\omega = n\Omega_{\mathrm{i0}}$. The Bessel sums retain all terms with index $|n| \leq 120$ to ensure convergence.

Figure 11 predicts that a larger region of the parameter space $(n_{\mathrm{cool}}/n_{\mathrm{hot}}, T_{\mathrm{cool}}/T_{\mathrm{hot}})$ becomes available to help stabilize DCLC in a BEAM-like concept. Complete stabilization $\mathrm{Im}(\omega) \to 0$ occurs when the cool plasma is a D/T mixture like the hot plasma, following the empirical "spectral rule" of[41]. For cool plasma of pure hydrogen, deuterium, or tritium, we find that $\mathrm{Im}(\omega)$ is reduced but generally remains non-zero; the remaining unstable modes have ω at the hot-ion cyclotron harmonics not overlapped by the cool-ion harmonics, as previously shown by[41].

Both[30] and[6] also computed the maximum radial gradient ϵ for DCLC to be stable, as a function of the density-proxy parameter $(\Omega_{\mathrm{i}}/\omega_{\mathrm{pi}})^2$. For WHAM, $\epsilon\rho_{\mathrm{i0}} \sim 1$ is DCLC unstable for nearly all values of $(\Omega_{\mathrm{i}}/\omega_{\mathrm{pi}})^2$ anyways. For the model BEAM plasma in Figure 11, we find $(\Omega_{\mathrm{i}}/\omega_{\mathrm{pi}})^2 \sim 3 \times 10^{-4}$ requires low $\epsilon\rho_{\mathrm{i0}} \sim 0.01$ for stability, so it is reasonable that our model with $|\epsilon\rho_{\mathrm{i0}}| \sim 0.04$ remains DCLC unstable in the absence of cool plasma.

Though Figure 11 suggests that a BEAM-like concept may be DCLC unstable, we note that many mitigating factors remain. First, BEAM-sized plasmas need much lower n_{cool} to stabilize DCLC as compared to WHAM, as expected from previous work[6]; there are many ways to craft such cool plasma in the laboratory. Second, the peaked beam-ion distributions used here may be viewed as "maximally" unstable; quasi-linear diffusion will smooth ion distributions towards marginal stability, as discussed in §3.4 and §4.1. Third, our calculation neglects physical effects such as finite plasma β (i.e., ∇B along r) and both radial and axial geometry; these effects are generally thought to aid stability[30]. Fourth, recall from Figure 9 that even if DCLC remains unstable, it can be rendered less harmful by pushing $\mathrm{Re}(\omega)$ to high harmonics of Ω_{i0} and so reducing DCLC's scattering rate, as shown on the GDT device[22]. Fifth, the plasma parameters in Figure 11 are only an example; no attempt was made, for this manuscript, to optimize parameter scan beyond what was discussed in[4]. Lastly, we recall that DCLC has been successfully mitigated in past and current mirror devices, including two that used WHAM/BEAM-like sloshing-ion injection: TMX-U and GDT. We will briefly discuss these real mirrors in §4.5.

As an aside: the 2D parameter-regime maps of Figures 9(a) and 11 show interesting structure that has been studied in detail by[35]; Gerver used a subtracted-Maxwellian distribution for hot ions, unlike our arbitrary beam-ion distributions, but his results agree qualitatively with ours. For example, Figure 11 shows that at low $T_{\mathrm{cool}}/T_{\mathrm{hot}}$, a distinct instability occurs even at large $n_{\mathrm{cool}}/n_{\mathrm{hot}} \gtrsim 10^{-1}$; it is called double-humped instability by[6][40] or ion two-temperature instability by[35]. The interested reader may consult[6][35][40][67] for more thorough treatments and reviews of DCLC linear-stability physics.

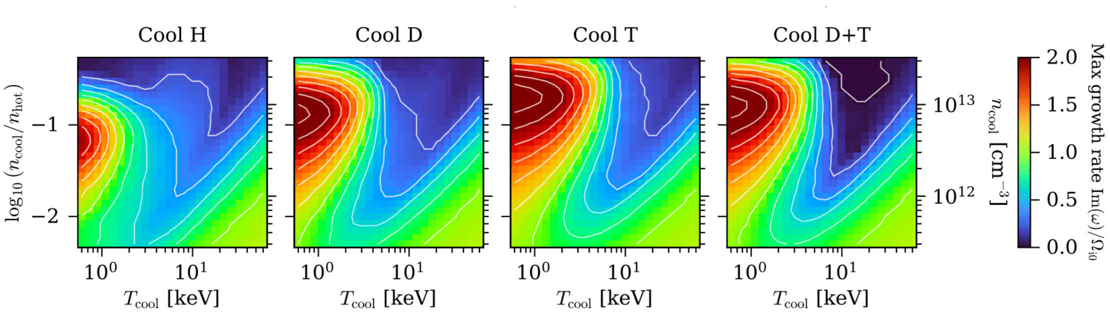

Figure 11. Effect of cool plasma on DCLC linear stability in a *physically-larger* next-step mirror, similar to the BEAM concept described in [4], with spatial gradient $|\epsilon|\rho_{\mathrm{i0}} = 0.04$ smaller than in WHAM. Each panel shows varying cool plasma composition. For the cool D+T case, n_{cool} counts both D/T species, and the cool D and cool T have equal densities. Total stabilization $\mathrm{Im}(\omega) \to 0$ is achieved when the cool ions' isotopes are matched to that of the hot ions. Colormap range in $\mathrm{Im}(\omega)$ is reduced from Figure 9(a).

4.3. Kinetic Electron Effects

Our linear dispersion relation assumed $k = k_{\perp}$, neglecting both ion and electron parallel responses. But, $k_{\|} \sim \pi/(2L_{\mathrm{p}})$ is imposed by the mirror geometry for the lowest possible axial harmonic. In WHAM with $R_{\mathrm{m}} = 20$, electrons with $T_{\mathrm{e}} \sim 1$ keV have thermal velocity v_{te} similar to DCLC parallel phase velocity $\omega/k_{\|} \sim \Omega_{\mathrm{i0}}/k_{\|}$, so DCLC modes may be Landau damped by electrons.

We qualitatively assess the effect of parallel electron kinetics in Equation 3.4 by replacing the perpendicular, cold-fluid electron susceptibility:

$$\chi_{\mathrm{e}} = \frac{\omega_{\mathrm{pe}}^2}{\Omega_{\mathrm{e}}^2} + \frac{\omega_{\mathrm{pe}}^2}{|\Omega_{\mathrm{e}}|} \frac{\epsilon}{k\omega} , \tag{4.1}$$

with a more general form for oblique electrostatic waves that includes a $\mathbf{B}$-parallel kinetic response:

$$\chi_{\mathrm{e}} = -\left(\frac{k_\perp}{k}\right)^2 \frac{\omega_{\mathrm{pe}}^2}{\Omega_{\mathrm{e}}^2} \left[1 + \frac{\epsilon|\Omega_{\mathrm{e}}|}{k_\perp \omega}\right] \zeta_{0\mathrm{e}} Z(\zeta_{0\mathrm{e}}) - \left(\frac{k_\parallel}{k}\right)^2 \frac{\omega_{\mathrm{pe}}^2}{k_\parallel^2 v_{\mathrm{te}}^2} Z'(\zeta_{0\mathrm{e}}) . \tag{4.2}$$

Here Z is the plasma dispersion function, $\zeta_{0\mathrm{e}} = \omega/(k_\parallel v_{\mathrm{te}})$, and $v_{\mathrm{te}} = \sqrt{2T_{\mathrm{e}}/m_{\mathrm{e}}}$. We fix $k_\parallel = \pi/(2L_{\mathrm{p}})$ to mimic a fundamental-harmonic mode along the device axis. Both Equations 4.1 and 4.2 are dimensionful. The derivation is briefly sketched in Appendix B.

Figure 12 re-computes DCLC linear stability, using Equation 4.2 to show the effect of parallel electron kinetics, for the ion distributions from our WHAM $R_m = 20$ simulation at $t = 0$ and $t = 6\,\tau_{\mathrm{bounce}} \approx 6\ \mu\mathrm{s}$. Figure 12(a) shows that the $t = 0$, peaked beam-ion distribution with empty loss cone remains unstable for a broad range of k; electron kinetics do not stabilize a strongly-peaked and hence strongly-unstable $F(v_\perp)$. In contrast, Figure 12(b) shows that the marginally-unstable $t = 6\ \mu\mathrm{s}$ distribution with filled loss cone has DCLC growth rates reduced by electron kinetics.

In the limit $T_{\mathrm{e}} \to \infty$, $\zeta_{0\mathrm{e}} \to 0$ suppresses the electron parallel susceptibility; i.e., the $(k_\parallel/k)^2$ term in Equation 4.2 asymptotes to $1/(k^2\lambda_{\mathrm{De}}^2)$, where λ_{De} is the electron Debye length, and its magnitude and contribution to D is negligible. More importantly, hot electrons and finite $k_\parallel$ suppress the *perpendicular* drift term in Equation 4.2 by driving $\zeta_{0\mathrm{e}} Z(\zeta_{0\mathrm{e}}) \to 0$; this disables the coupling between ion Bernstein waves and the drift wave. In Figure 12(b), at $T_{\mathrm{e}} \gtrsim 100\ \mathrm{keV}$ the electrostatic mode structure appears similar to the "pure" ion Bernstein waves in a homogeneous plasma, but with a non-zero growth rate that we speculate may arise from negative-energy wave destabilization in the presence of a Landau damping term[6][68][69].

In the limit of low $T_{\mathrm{e}} \lesssim 1$ keV, the perpendicular drift term in Equation 4.2 reverts to its fluid form because $\zeta_{0\mathrm{e}} Z(\zeta_{0\mathrm{e}}) \to -1$. The parallel term, which asymptotes to $-(k_\parallel/k)^2(\omega_{\mathrm{pe}}/\omega)^2$, is the main new influence on DCLC mode structure. Figure 6(a) shows that the $t = 0$ beam-ion distribution is not much affected at low T_{e} when compared to Figure 6(j). But, Figure 12(b) shows that the $t = 6\ \mu\mathrm{s}$ distribution has low harmonics of DCLC suppressed, and the growth rates of higher harmonics somewhat reduced, by electron kinetics when compared to Figure 6(g).

Equation 4.2 is less accurate than bounce averaging of unperturbed particle orbits within a specified axial mirror geometry, as has been performed and studied by, e.g.,[16][38], and others. A significant unknown is the effect of the non-monotonic axial electric potential ϕ; since $\phi \sim T_\mathrm{e}$ and ϕ can trap electrons at sloshing-ion turning points, electron orbits may be significantly modified. None of this is captured in our Hybrid-VPIC simulations given the simple electron closure. Our goal is only to show qualitatively how parallel electron kinetics, including electron Landau damping, may impact DCLC. We conclude that saturated DCLC amplitude and frequency in WHAM may be tunable via T_e or other device parameters, as was done on the MIX-1 device previously[16][70].

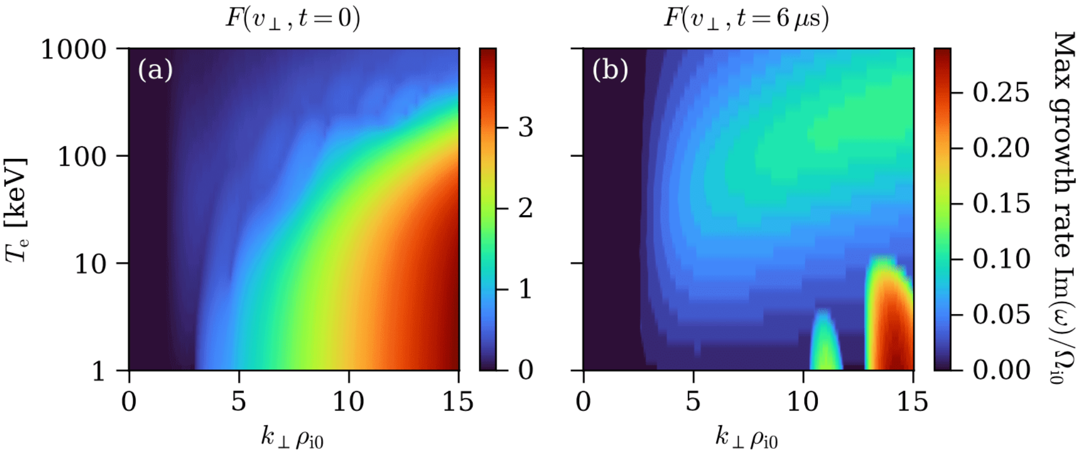

Figure 12. Effect of parallel-kinetic electron response upon DCLC linear stability, using ion distributions from the WHAM $R_m = 20$ simulation at either $t = 0$ to obtain a beam-ion distribution (left), or at $t = 6\ \mu$s to obtain a saturated distribution with $\mathrm{d}F/\mathrm{d}v_\perp < 0$ (right).

4.4. Other Modes

Our simulations mostly grow DCLC, but other kinetic and fluid modes can appear in mirror devices[67]. The modes relevant to WHAM were surveyed by[1]; here we add a few remarks.

Interchange modes should be stabilized by the effect of finite ion Larmor radius (FLR), specifically collisionless gyroviscosity[71], when

$$k_\perp \rho_\mathrm{i0} > 4\sqrt{\frac{a}{L_\mathrm{p}}} \approx 1.3\,, \tag{4.3}$$

with $a \approx 10\ \mathrm{cm}$ the plasma column radius and assuming a curvature-driven growth rate $v_{\mathrm{ti0}}/\sqrt{aL_{\mathrm{p}}}$ [72]. In Figure 13, we present new simulations of Maxwellian ions with varying temperature $T_{\mathrm{i0}} = 5$ to $20\ \mathrm{keV}$ in the WHAM $R_{\mathrm{m}} = 20$ geometry. As T_{i0} decreases, DCLC weakens in amplitude and spectral width, and a lower-m mode grows in amplitude and spectral width. We identify the lower-m mode as interchange because (i) its phase velocity is half the ion diamagnetic drift and in the same direction (neglecting gravitational drift, which is $\sim(a/L_{\mathrm{p}})\times$ smaller), consistent with the planar-slab derivation[71][73], (ii) its k bandwidth qualitatively scales with T_{i} following Equation 4.3. Note that in this paragraph and Figure 13, we redefine $v_{\mathrm{ti0}} = \sqrt{2T_{\mathrm{i0}}/m_{\mathrm{i}}}$ with a factor of $\sqrt{2}$, which also affects $\rho_{\mathrm{i0}} = v_{\mathrm{ti0}}/\Omega_{\mathrm{i0}}$. We caution that our simulated interchange has relatively strong $m = 2$ and $m = 4$ modes compared to, e.g., the odd $m = 3$ mode; this effect may be unphysical, and we suspect mesh imprinting.

Alfvén ion cyclotron (AIC) modes do not appear at significant amplitude in our simulations; recall that both δB_r and δB_θ are small (§3.1), and pitch-angle scattering is weak compared to DCLC's $v_\perp$ scattering (Figure 3). Does our non-observation agree with theory and prior experiments? An empirical criterion for AIC growth, obtained from experiments on the tandem mirror GAMMA-10[74][75], is

$$T_{\mathrm{i}\perp}/T_{\mathrm{i}\|} > 0.55/\beta_\perp^{0.5}\,, \tag{4.4}$$

based on data with $\beta_\perp < 0.03$. One linear-instability criterion, derived for a homogeneous bi-Maxwellian plasma[76] and with a form commonly used in solar-wind literature[77], is:

$$T_{\mathrm{i}\perp}/T_{\mathrm{i}\|} > 1 + 0.43/\beta_\|^{0.42}\,. \tag{4.5}$$

At $t = 0$ in our $R_{\mathrm{m}} = 20$ simulation, the sloshing-ion turning points have $\beta_\perp = 8\pi n k_{\mathrm{B}} T_{\mathrm{i}\perp}/B^2 = 0.17$ and $\beta_\| = 8\pi n k_{\mathrm{B}} T_{\mathrm{i}\|}/B^2 = 0.068$, with corresponding anisotropy $T_{\mathrm{i}\perp}/T_{\mathrm{i}\|} = 2.5$; our simulations with larger R_{m} have similar anisotropy and lower plasma beta at the turning points. Both Equations 4.4 and 4.5 indicate that AIC may be unstable at the turning points.

So, why does AIC not appear? First, since AIC is driven by gradients of f on resonant surfaces in velocity space, Equations 4.4 and 4.5 will not be so precise when applied to different ion distributions; e.g.,[78] noted that subtle modifications to f at marginal AIC stability can modify anisotropy thresholds based on bi-Maxwellian temperatures by a factor of ~ 2. Second, AIC is stabilized by the inhomogeneous plasma in WHAM. Sloshing ions put perpendicular pressure anisotropy at turning points, so instability drive weakens towards the mirror cell's center. A small plasma column radius with respect to the ion Larmor radius also aids stability[79]. And, AIC is suppressed if the mirror's axial length is shorter than a critical length[80][81][82]:

$$L_\mathrm{c} = 2\pi^2 \sqrt{\frac{T_{\mathrm{i}\parallel}}{\beta_\perp T_{\mathrm{i}\perp}}} \left(\frac{c}{\omega_\mathrm{pi}} \right) . \tag{4.6}$$

The critical length $L_\mathrm{c} \approx 182\ \mathrm{cm}$ is very close to WHAM's length $2L_\mathrm{p} = 196\ \mathrm{cm}$, again taking $\beta_\perp = 0.17$ and assuming $c/\omega_\mathrm{pi} = 5.9\ \mathrm{cm}$ for density $n = 3 \times 10^{13}\ \mathrm{cm}^{-3}$ at sloshing-ion turning points. Third, DCLC simply has a faster growth rate and decreases plasma beta before AIC can be triggered.

To summarize: AIC with low axial mode number may be marginally unstable for WHAM, based on the highest possible $\beta_\perp$ and density n at sloshing-ion turning points. But multiple effects weaken AIC drive and so may explain why it does not appear in our simulations.

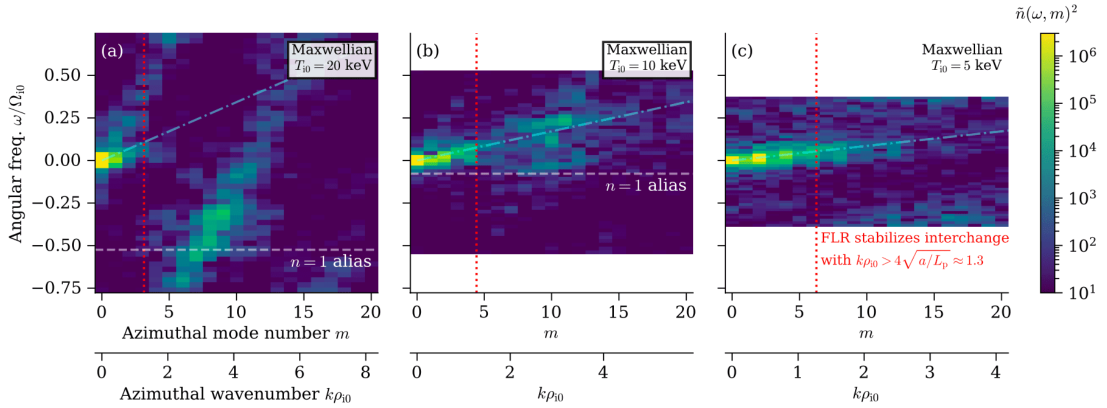

Figure 13. Interchange modes appear and DCLC weakens as T_i decreases (left to right) in simulations of Maxwellian ions in WHAM's $R_\mathrm{m} = 20$ magnetic-field geometry. Fourier spectra computed as in Figure 6. The dot-dashed cyan line plots the interchange mode's expected phase velocity, $\omega/k = v_{\mathrm{Di}}/2$, assuming spatial gradient $\epsilon = (10\mathrm{cm})^{-1}$.

4.5. Comparison to Real Mirrors

In the TMX-U end-plugs with sloshing ion injection, it was possible to stabilize DCLC fluctuations and obtain "classical mirror confinement", i.e., an ideal mirror performance regime wherein particle losses are due solely to Coulomb collisions[13][14]. Such DCLC stabilization may be attributed to cool ions trapped by the sloshing ions' non-monotonic axial electrostatic potential[27]. But, DCLC-scattered beam ions enter the loss cone with large $v_{\|}$ and are not trapped; therefore, trapped cool ions must come from other sources. In a tandem mirror like TMX-U, central-cell outflow into end-plugs can provide cool ions. In any real laboratory experiment, charge exchange of beam ions upon a neutral background population will also provide a population of cool ions. Both TMX-U and GDT found operating parameters where DCLC fluctuations were quelled by the (inferred) presence of cold plasma; we especially call attention to recent GDT measurements in Figure 4(b,d) of[22]. A combination of (i) future full-device kinetic-ion simulations with better models of fueling and collisions, e.g. via two-way coupling between Hybrid-VPIC and CQL3D-m over a $20\ \mathrm{ms}$ laboratory shot duration, and (ii) real experimental data from WHAM, can more definitively test the efficacy of DCLC stabilization by cool ion populations.

In real mirror devices, discrete DCLC modes can persist stably for $\sim\mathcal{O}(1\ \mathrm{ms})$[22], but DCLC can also appear as discrete bursts of enhanced fluctuations with duration ~ 10 to $100\ \mu\mathrm{s}$[11][20][22]. Our simulations do not show bursting, nor did previous simulations by[38].[20] explained bursty DCLC in the GAMMA-6A experiment using a quasi-linear model with bounce-averaged electron Landau damping; they appealed to (i) separation between DCLC scattering and axial outflow timescales (i.e., $1/\nu_{\perp\perp} \ll \tau_{\mathrm{GD}}$), and (ii) fast time variation in DCLC growth rate with slower variation in electron-Landau damping rate. More broadly, bursting behavior should be sensitive to any mirror parameters that alter DCLC growth/damping rates with respect to τ_{GD} (e.g., T_{e}, $\omega_{\mathrm{pi}}/\Omega_{\mathrm{i}}$, external particle fueling or heating). In our simulations, $1/\nu_{\perp\perp} \sim \tau_{\mathrm{GD}}$ at order of magnitude (Figure 8(b)), and DCLC appears marginally stable and does not damp on a timescale $\ll \tau_{\mathrm{GD}}$.

TMX-U and GDT saw that DCLC could be driven at sloshing-ion turning points instead of at the mirror mid-plane $z = 0$[14][22]; Why does DCLC have strongest drive at $z = 0$, versus at the turning points, in our simulations of WHAM? In TMX-U, the end-plug could be stabilized on one side and not the other due to a combination of axial flows from the central cell and localized ECH at the end-plug outer-turning point. As for GDT versus WHAM, we cannot answer definitively, but we note that WHAM's axial length $\approx 2\ \mathrm{m}$ may constrain DCLC's unstable axial eigenmodes as compared to the longer GDT ($7\ \mathrm{m}$).

WHAM began operating in July 2024[83]. A comparison between experimental data and our simulations is not yet available. We anticipate that WHAM plasmas and diagnostics may be tuned to create and measure DCLC modes in future experimental campaigns.

5. Conclusions

We have performed 3D kinetic-ion simulations of WHAM, initialized with a neutral-beam-injected deuteron population with $T_\mathrm{i} \sim 10~\mathrm{keV}$ and cool, isothermal-fluid electrons with $T_\mathrm{e} \sim 1~\mathrm{keV}$, to assess kinetic plasma stability in a high-performance, collisionless-ion regime. We find that WHAM's beam-ion distribution is unstable to an electrostatic, flute-like ($k \approx k_\perp$) mode that grows on $\lesssim 1~\mu\mathrm{s}$ timescales; it propagates azimuthally around the column in the ion diamagnetic direction and has angular frequency between Ω_i0 and $2\Omega_\mathrm{i0}$. We identify it as the drift-cyclotron loss cone (DCLC) mode, well known from prior mirror experiments[11] and previously anticipated to be a possible concern for WHAM[1].

The plasma column and DCLC fluctuations settle into a steady-state decay by $t = 6~\mu\mathrm{s}$. Particles escape axially with confinement time $\tau_\mathrm{p} = n/(\mathrm{d}n/\mathrm{d}t) \sim 10^2~\mu\mathrm{s}$ in a "gas dynamic" regime, wherein the scattering rate into the loss cone equals or exceeds the free-streaming axial transit time out of the mirror. Particle losses are due to collisionless $v_\perp$ scattering upon the DCLC modes; the particle-wave correlation time is approximately ${\Omega_\mathrm{i0}}^{-1}$ at the mirror mid-plane. Particle losses and velocity-space diffusion are strongest at the plasma's radial edge, whereas the plasma column's core can maintain $\mathrm{d}F/\mathrm{d}v_\perp > 0$ at low velocities. We review well-known and experimentally-tested methods for stabilizing DCLC: addition of cool plasma to fill the loss cone, larger plasma extent (smaller gradient), and parallel electron kinetics including Landau damping. In 3D simulations with cool ions initialized at the plasma's radial edge, the particle confinement time can be raised by a factor of 2 to $5\times$, though an order-unity ratio of cool/hot ion number density is needed. In a real experiment, the cool ions must be provided by external sources because DCLC does not scatter beam ions into the axial electrostatic potential well (aka Yushmanov potential) where they could be trapped to help stabilize DCLC. DCLC-scattered beam ions are lost because they retain large parallel speeds and so never enter the trapped region of phase space.

Our simulations are limited, primarily in the electric field model and isothermal-fluid electron closure. Future work may incorporate electron inertia, an electron energy equation, drift-kinetic electrons, or more to help model (i) bounce-averaged electron Landau damping, and (ii) the plasmas' axial and radial potential structure, which dictate outflows and rotation. And, the initial condition of a hot, beam-ion plasma with only mild slowing-down upon electrons is somewhat idealized. Other subsystems on WHAM are not modeled, e.g., heating of ions and electrons via RF and microwave radiation respectively, or biased end-rings within the expanders used to drive rotation and shear flow. Collisions with neutral atoms can also generate cool plasma. Future work may also consider a wider range of fueling and heating scenarios in WHAM and next-step mirror devices.

Appendix A. Hyper-Resistivity Scan

Hyper-resistivity, although intended to suppress grid-scale numerical noise, may also alter DCLC mode structure as discussed in §2.2. Figure 14 shows that raising or decreasing η_{H} by a factor of 3 alters the spectrum of density fluctuations at the plasma edge; with higher η_{H}, the spectrum broadens and is less coherent.

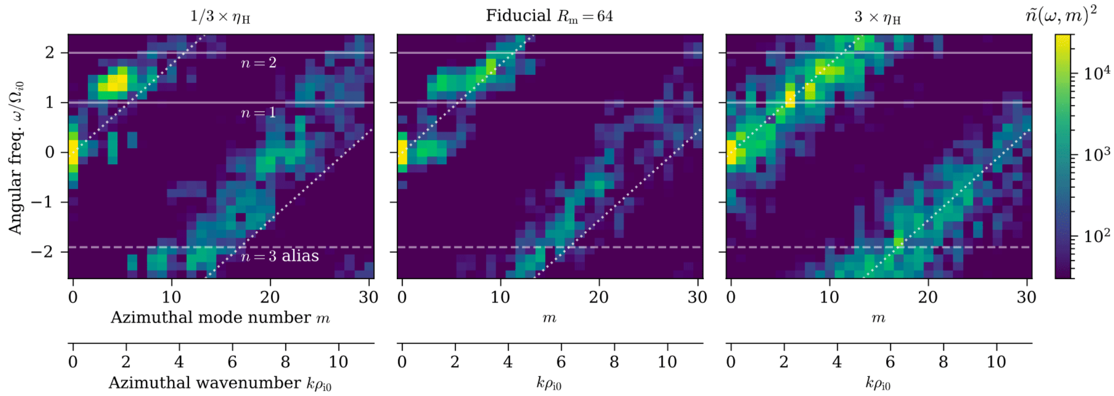

Figure 14. Effect of hyper-resistivity, increasing left to right, upon density-fluctuation Fourier spectra in WHAM $R_{\mathrm{m}} = 64$ simulations; center panel is same data as Figure 6(c). Fourier spectra and annotations constructed like in Figure 6, at same $r = 2.69\rho_{\mathrm{i0}}$ over $t = 3$ to $6\ \tau_{\mathrm{bounce}}$, but the colormap range and 2D plot domain/range are changed.

Appendix B. Electron Parallel Response

To obtain the electrons' parallel response in §4.3, we start again from[84], §14-3, Eq. (8), neglecting spatial derivatives of order $\partial^2 g/\partial y^2$ or higher in Stix's notation, where g is the guiding-center distribution. For a Maxwellian guiding-center distribution, the susceptibility is:

$$\chi_{\mathrm{s}} = \left(\frac{\omega_{ps}}{\Omega_{\mathrm{s}}}\right)^2 \sum_{n=-\infty}^{\infty} e^{-\lambda} I_n(\lambda) \Bigg\{ \left(\frac{k_\perp}{k}\right)^2 \left[\frac{2n}{k_\perp^2}\left(1 - \frac{n\epsilon}{k_\perp}\right) + \frac{\epsilon}{k_\perp}\right] \frac{Z(\zeta_n)}{k_\parallel} + \left(\frac{k_\parallel}{k}\right)^2 \frac{2}{k_\parallel^2}\left(1 - \frac{n\epsilon}{k_\perp}\right) \left[1 + \zeta_n Z(\zeta_n)\right] \Bigg\}, \tag{B1}$$

where the modified Bessel function $I_n(\lambda)$ has argument $\lambda = k_\perp^2/2$, the plasma dispersion function $Z(\zeta_n)$ has argument $\zeta_n = (\omega - n)/k_\parallel$, and the variables $\omega, \epsilon, k, k_\perp, k_\parallel$ are all dimensionless following the same *species-specific* scheme used for Equation 3.3. Equation B1 is valid for any $\boldsymbol{k}$ angle. The limit $\zeta_n \to \infty$ and $k_\parallel/k \to 0$ recovers the perpendicular susceptibility given by Equation 3.3. The limit $\epsilon/k_\perp \to 0$ recovers the standard[85] dispersion relation[86].

Let us simplify Equation B1 by taking the limits $k \to 0$ and $\omega \to 0$, and further keep only the $n = 0$ and ± 1 Bessel terms. In the ensuing expansion, it follows that $\zeta_{\pm 1} = (\omega \mp 1)/k_\parallel \approx \mp 1/k_\parallel \to \infty$, but we make no assumptions on the magnitude of $\zeta_0 = \omega/k_\parallel$. The result is:

$$\chi_{\mathrm{s}} = \left(\frac{\omega_{\mathrm{p}s}}{\Omega_{\mathrm{s}}}\right)^2 \left\{ \left(\frac{k_\perp}{k}\right)^2 \left[\frac{\epsilon}{k_\perp \omega} - 1\right] \zeta_0 Z(\zeta_0) + \left(\frac{k_\parallel}{k}\right)^2 \frac{2}{k_\parallel^2} [1 + \zeta_0 Z(\zeta_0)] \right\} . \tag{B2}$$

which yields Equation 3.2 after putting in dimensions. The limit $\zeta_0 \to \infty$ recovers the familiar cold-fluid result, written below in dimension-*ful* variables:

$$\chi_{\mathrm{s}} = \left(\frac{k_\perp}{k}\right)^2 \frac{\omega_{\mathrm{p}s}^2}{\Omega_{\mathrm{s}}^2} \left[1 - \frac{\epsilon \Omega_{\mathrm{s}}}{k_\perp \omega}\right] - \left(\frac{k_\parallel}{k}\right)^2 \frac{\omega_{\mathrm{p}s}^2}{\omega^2} . \tag{B3}$$

A subtlety appears when expanding Equation B1 into EquationB2. Consider the susceptibility tensor components $\chi_{\perp\perp}$ and $\chi_{\parallel\parallel}$ for a hot homogeneous plasma[84]. The perpendicular response simplifies in the cold-fluid limit:

$$\chi_{\perp\perp} \to \frac{\omega_{\mathrm{p}s}^2}{\Omega_{\mathrm{s}}^2} . \tag{B4}$$

But, $\chi_{\perp\perp}$ is *cancelled* by the analogous expansion of $\chi_{\parallel\parallel}$ when (i) both $k_\perp$ and $k_\parallel$ are finite, (ii) ζ_0 is kept finite, and (iii) terms of order $\mathcal{O}(\lambda^1)$ are kept in expanding $e^{-\lambda} I_0(\lambda)$. Said expansion gives:

$$\begin{aligned} \chi_{\parallel\parallel} &\to \frac{\omega_{\mathrm{p}s}^2}{\Omega_{\mathrm{s}}^2} \frac{2}{k_\parallel^2} [1 + \zeta_0 Z(\zeta_0)] \left(1 - \lambda + \mathcal{O}(\lambda^2)\right) \\ &= \frac{\omega_{\mathrm{p}s}^2}{\Omega_{\mathrm{s}}^2} \left\{ \frac{2}{k_\parallel^2} [1 + \zeta_0 Z(\zeta_0)] - \frac{k_\perp^2}{k_\parallel^2} - \frac{k_\perp^2}{k_\parallel^2} \zeta_0 Z(\zeta_0) \right\} , \end{aligned} \tag{B5}$$

with $k_\parallel$ dimensionless as before. Then, in the combined electrostatic susceptibility

$$\chi \approx (k_\perp/k)^2 \chi_{\perp\perp} + (k_\parallel/k)^2 \chi_{\parallel\parallel} + (2 k_\parallel k_\perp / k^2) \chi_{\perp\parallel} , \tag{B6}$$

we see that Equations B4 and B5 partly cancel, and only a *parallel* contribution $-(k_\perp/k)^2 (\omega_{\mathrm{p}s}/\Omega_{\mathrm{s}})^2 \zeta_0 Z(\zeta_0)$ remains. This remainder term can be seen in Equation B2. When the $\zeta_0 \to \infty$ limit is taken, it is this parallel remainder that provides the usual perpendicular response

$\chi_{\perp\perp} \to \omega_{\mathrm{p}s}^2/\Omega_{\mathrm{s}}^2$. This is to some extent a semantic quibble; we can also say that the remainder term $-(k_\perp/k)^2(\omega_{\mathrm{p}s}/\Omega_{\mathrm{s}})^2\zeta_0 Z(\zeta_0)$ cancels the parallel term $-(k_\perp/k)^2(\omega_{\mathrm{p}s}/\Omega_{\mathrm{s}})^2$ to leave only the perpendicular term $+(k_\perp/k)^2(\omega_{\mathrm{p}s}/\Omega_{\mathrm{s}})^2$ in Equation B6. But, the overall point stands that the perpendicular term in Equation B2 can be significantly modified by the parallel response, even when $k_\| \ll k_\perp$; the regulating parameter is ζ_0.

Statements and Declarations

Acknowledgements

Conversations with Mana Francisquez, Erik Granstedt, Mark Koepke, Dmitri Ryutov, Dmitry Yakovlev, Mason Yu, and the entire WHAM team are gratefully acknowledged.

Funding

Funding for this work was provided by Realta Fusion, the U.S. Department of Energy (DOE), and the U.S. National Science Foundation (NSF). WHAM collaboration work is supported by the U.S. DOE through ARPA-E DE-AR0001258, Commonwealth Fusion Systems, Realta Fusion, Wisconsin Alumni Research Foundation, and a lengthy list of collaborators providing valuable equipment. AT was partly supported by NSF PHY-2010189 and the DOE Fusion Energy Sciences Postdoctoral Research Program, administered by the Oak Ridge Institute for Science and Education (ORISE) and Oak Ridge Associated Universities (ORAU) under DOE contract DE-SC0014664.

High-performance computing resources were provided by the National Energy Research Scientific Computing Center (NERSC), a DOE Office of Science User Facility, via allocation FES-ERCAP0026655; Anvil at Purdue University's Rosen Center for Advanced Computing[87][88] via allocation PHY230179 from the NSF Advanced Cyberinfrastructure Coordination Ecosystem: Services & Support (ACCESS) program; Amazon Web Services' Compute for Climate Fellowship awarded to Realta Fusion; Los Alamos Institutional Computing; and UW–Madison's Center for High Throughput Computing[89]. ACCESS[90] is supported by NSF grants #2138259, #2138286, #2138307, #2137603, and #2138296.

All opinions expressed in this paper are the authors' and do not necessarily reflect the policies and views of DOE, ORAU, or ORISE.

Conflicts of interest

C. B. Forest is a co-founder of Realta Fusion; D. A. Endrizzi, S. J. Frank, and J. Viola are employees of Realta Fusion. This work was partly supported by a grant from Realta Fusion to the University of Wisconsin–Madison.

Footnotes

[1] Publicly available at https://github.com/lanl/vpic-kokkos/tree/hybridVPIC.

[2] If hyper-resistivity were used to model electron-ion friction, and no explicit collision operator for ions is used, only the frictionless $\mathbf{E}$ should be used in the ion push[[91], Appendix A].

[3] The 250 eV temperature is higher than in experiments so that we can use coarser velocity-space grid resolution. The final evolved solution varies little with initial temperature.

[4] https://github.com/eepeterson/pleiades

[5] We checked that Equation 3.6 does not cause noticeable selection bias for short $\delta t \lesssim \Omega_{i0}^{-1}$; radial profiles of $\langle \delta v_\perp \rangle$ and $\langle \delta v_\perp \delta v_\perp \rangle$, computed with and without particles excluded by Equation 3.6, appear identical to the eye. For larger δt, particles accumulate order-unity kicks in $v_\perp$ and selection bias appears.

References

1. a, b, c, d, e, f *D. Endrizzi, J. K. Anderson, M. Brown, J. Egedal, B. Geiger, et al. (2023). Physics basis for the Wisconsin HTS Axisymmetric Mirror (WHAM). Journal of Plasma Physics. 89(5):975890501. doi:10.1017/S0022377823000806*
2. ^ *T. Simonen, R. Cohen, D. Correll, K. Fowler, D. Post, et al. (2008). The axisymmetric tandem mirror: A magnetic mirror concept game changer magnet mirror status study group. Lawrence Livermore National Laboratory 2008. Report No.: LLNL-TR-408176. doi:10.2172/945844*
3. ^ *P. A. Bagryansky. (2024). Progress of open systems at Budker Institute of Nuclear Physics. Journal of Plasma Physics. 90(2):905900218. doi:10.1017/S0022377824000473*
4. a, b, c, d, e, f, g *C. B. Forest, J. K. Anderson, D. Endrizzi, J. Egedal, S. Frank, et al. (2024). Prospects for a high-field, compact break even axisymmetric mirror (BEAM) and applications. submitted to Journal of Plasma Physics.*

5. a, b*R. F. Post, M. N. Rosenbluth. (1966). Electrostatic Instabilities in Finite Mirror-Confined Plasmas. Physics of Fluids. 9(4):730–749. doi:10.1063/1.1761740*
6. a, b, c, d, e, f, g, h, i*D. E. Baldwin. (1977). End-loss processes from mirror machines. Reviews of Modern Physics. 49(2):317–339. doi:10.1103/RevModPhys.49.317*
7. ^*A. B. Mikhailovskii, A. V. Timofeev. (1963). Theory of Cyclotron Instability in a Non-Uniform Plasma. Sov Phys JETP. 17(3):626.*
8. ^*Ju. T. Bajborodov, M. S. Ioffe, B. I. Kanaev, R. I. Sobolev, E. E. Jushmanov. (1971). Investigation of Plasma Decay in the PR-6 Adiabatic Trap. In: Proceedings of the fourth international conference on plasma physics and controlled nuclear fusion research.: Vienna: International Atomic Energy Agency (IAEA).*
9. a, b*M. S. Ioffe, B. I. Kanaev, V. P. Pastukhov, E. E. Yushmanov. (1975). Stabilization of cone instability of collisional plasma in a mirror trap. Soviet Journal of Experimental and Theoretical Physics. 40(6):1064–1069.*
10. ^*V. V. Piterskiĭ, E. E. Yushmanov, A. N. Yakovets. (1995). Stabilization of the drift-cone instability by a flow shear. Soviet Journal of Experimental and Theoretical Physics Letters. 62:303.*
11. a, b, c, d, e*F. H. Coensgen, W. F. Cummins, B. G. Logan, A. W. Molvik, W. E. Nexsen, et al. (1975). Stabilization of a Neutral-Beam-Sustained, Mirror-Confined Plasma. 35(22):1501–1503. doi:10.1103/PhysRevLett.35.1501*
12. a, b*R. P. Drake, T. A. Casper, J. F. Clauser, F. H. Coensgen, D. L. Correll, et al. (1981). The effect of end-cell stability on the confinement of the central-cell plasma in TMX. Nuclear Fusion. 27:359–364.*
13. a, b, c*T. C. Simonen, S. L. Allen, T. A. Casper, J. F. Clauser, C. A. Clower, et al. (1983). Operation of the tandem-mirror plasma experiment with skew neutral-beam injection. 50(21):1668–1671. doi:10.1103/PhysRevLett.50.1668*
14. a, b, c, d*L. V. Berzins, T. A. Casper. (1987). Ion microinstability at the outer sloshing-ion turning point of the tandem mirror experiment upgrade (TMX-U). 59(13):1428–1431. doi:10.1103/PhysRevLett.59.1428*
15. a, b, c*John R. Ferron, Alfred Y. Wong. (1984). The dependence of the drift cyclotron loss cone instability on the radial density gradient. Physics of Fluids. 27(5):1287–1300. doi:10.1063/1.864745*
16. a, b, c, d*M. Koepke, R. F. Ellis, R. P. Majeski, M. J. McCarrick. (1986). Experimental observation of bounce-resonance Landau damping in an axisymmetric mirror plasma. 56(12):1256–1259. doi:10.1103/PhysRevLett.56.1256*
17. ^*M. Koepke, M. J. McCarrick, R. P. Majeski, R. F. Ellis. (1986). Three-dimensional mode structure of the drift cyclotron loss-cone instability in a mirror trap. Physics of Fluids. 29(10):3439–3444. doi:10.1063/1.8*

65860

18. ^*M. J. McCarrick, J. H. Booske, R. F. Ellis. (1987). Observations of the dependence of unstable drift cyclotron loss cone mode characteristics on plasma density. Physics of Fluids. 30(2):614–617. doi:10.1063/1.866363*
19. ^*G. R. Burkhart, P. N. Guzdar, M. E. Koepke. (1989). Theoretical modeling of drift cyclotron loss-cone instability mode structures. Physics of Fluids B. 1(3):570–580. doi:10.1063/1.859117*
20. a, b, c*Hiroyuki Yamaguchi. (1996). Amplitude Oscillation of an Instability in a Plasma in the Presence of a Damping Mechanism. Journal of the Physical Society of Japan. 65(10):3115. doi:10.1143/JPSJ.65.3115*
21. a, b*V. V. Prikhodko, P. A. Bagryansky, E. D. Gospodchikov, A. A. Lizunov, Z. E. Konshin, et al. (2018). Stability and Confinement Studies in the Gas Dynamic Trap. In: 27th IAEA fusion energy conference, gandhinagar, india. pp. IAEA-CN-258/EX/P5-25.*
22. a, b, c, d, e, f, g, h, i*Evgeniy A. Shmigelsky, Andrey K. Meyster, Ivan S. Chernoshtanov, Andrej A. Lizunov, Alexander L. Solomakhin, et al. (2024). Kinetic instabilities in two-isotopic plasma in the GDT magnetic mirror. submitted to Journal of Plasma Physics.*
23. ^*B. I. Kanaev. (1979). Stabilization of drift loss-cone instability /DCI/ by addition of cold ions. Nuclear Fusion. 19:347–359.*
24. a, b*D. L. Correll, J. H. Clauser, F. H. Coensgen, W. F. Cummins, R. P. Drake, et al. (1980). Production of large-radius, high-beta, confined mirror plasmas. Nuclear Fusion. 20:655–664.*
25. ^*E. E. Yushmanov. (1966). Confinement of Slow Ions of a Plasma with Positive Potential in a Mirror Trap. Soviet Journal of Experimental and Theoretical Physics. 22:409.*
26. ^*J. Kesner. (1973). Inverse ambipolar potential in a magnetic mirror configuration. Plasma Physics. 15(6):577–584. doi:10.1088/0032-1028/15/6/009*
27. a, b*J. Kesner. (1980). Axisymmetric sloshing-ion tandem-mirror plugs. Nuclear Fusion. 20:557–562.*
28. ^*Richard F. Post. (2003). The Kinetic Stabilizer: Further Calculations and Options. Fusion Science and Technology. 43(1T):195–202. doi:10.13182/FST03-A11963593*
29. ^*T. K. Fowler, R. W. Moir, T. C. Simonen. (2017). A new simpler way to obtain high fusion power gain in tandem mirrors. Nuclear Fusion. 57(5):056014. doi:10.1088/1741-4326/aa5e54*
30. a, b, c, d*W. M. Tang, L. D. Pearlstein, H. L. Berk. (1972). Finite Beta Stabilization of the Drift-Cone Instability. Physics of Fluids. 15(6):1153–1155. doi:10.1063/1.1694044*
31. ^*Muhammad Bashir Chaudhry. (1983). Electrostatic Drift Ion Cyclotron Waves in Sheet Plasmas with and without Ambipolar Field. Journal of the Physical Society of Japan. 52(3):856. doi:10.1143/JPSJ.52.856*

32. ^*H. Sanuki, R. D. Ferraro. (1986). Nonlocal Theory of DCLC Modes in a Plasma Slab with an Ambipolar Field. 34(1):58–62. doi:10.1088/0031-8949/34/1/010*
33. a, b*R. E. Aamodt. (1977). Electron stabilization of drift-cone modes. Physics of Fluids. 20(6):960–962. doi:10.1063/1.861983*
34. ^*Akira Hasegawa. (1978). Stabilization of Drift-Cyclotron Loss-Cone Mode by Low-Frequency Density Fluctuations. 40(14):938–941. doi:10.1103/PhysRevLett.40.938*
35. a, b, c, d*M. J. Gerver. (1976). Stabilization of drift cyclotron loss cone instability with additions of small amounts of cool plasma. Physics of Fluids. 19(10):1581–1590. doi:10.1063/1.861363*
36. a, b, c*N. E. Lindgren, C. K. Birdsall, A. B. Langdon. (1976). Electrostatic waves in an inhomogeneous collisionless plasma. Physics of Fluids. 19(7):1026–1034. doi:10.1063/1.861572*
37. a, b*Bruce I. Cohen, Neil Maron, Gary R. Smith. (1982). Some nonlinear properties of drift-cyclotron modes. Physics of Fluids. 25(5):821–841. doi:10.1063/1.863812*
38. a, b, c, d*Bruce I. Cohen, Gary R. Smith, Neil Maron, William McCay Nevins. (1983). Particle simulations of ion-cyclotron turbulence in a mirror plasma. Physics of Fluids. 26(7):1851–1865. doi:10.1063/1.864362*
39. a, b*R. D. Ferraro, R. G. Littlejohn, H. Sanuki, B. D. Fried. (1987). Nonlocal effects on the drift cyclotron loss cone dispersion relation in cylindrical geometry. Physics of Fluids. 30(4):1115–1122. doi:10.1063/1.866310*
40. a, b, c, d*Igor A. Kotelnikov, Ivan S. Chernoshtanov, Vadim V. Prikhodko. (2017). Electrostatic instabilities in a mirror trap revisited. Physics of Plasmas. 24(12):122512. doi:10.1063/1.5013059*
41. a, b, c*Igor A. Kotelnikov, Ivan S. Chernoshtanov. (2018). Isotopic effect in microstability of electrostatic oscillations in magnetic mirror traps. Physics of Plasmas. 25(8):082501. doi:10.1063/1.5036816*
42. ^*D. E. Baldwin, H. L. Berk, L. D. Pearlstein. (1976). Turbulent Lifetimes in Mirror Machines. 36(17):1051–1054. doi:10.1103/PhysRevLett.36.1051*
43. ^*H. L. Berk, J. J. Stewart. (1977). Quasi-linear transport model for mirror machines. Physics of Fluids. 20(7):1080–1088. doi:10.1063/1.861994*
44. ^*R. E. Aamodt, Y. C. Lee, C. S. Liu, M. N. Rosenbluth. (1977). Nonlinear dynamics of drift-cyclotron instability. 39(26):1660–1663. doi:10.1103/PhysRevLett.39.1660*
45. ^*R. C. Myer, A. Simon. (1980). Nonlinear saturation of the drift cyclotron loss-cone instability. Physics of Fluids. 23(5):963–973. doi:10.1063/1.863069*
46. ^*B. I. Cohen, N. Maron. (1980). Simulation of drift-cone modes. Physics of Fluids. 23(5):974–980. doi:10.1063/1.863070*

47. ^R. E. Aamodt, B. I. Cohen, Y. C. Lee, C. S. Liu, D. R. Nicholson, et al. (1981). *Nonlinear evolution of drift cyclotron modes. Physics of Fluids. 24(1):55–65. doi:10.1063/1.863246*
48. ^Bruce I. Cohen, Neil Maron, William McCay Nevins. (1984). *Simulation of drift-cyclotron-loss-cone modes in tandem mirrors with sloshing ions. Physics of Fluids. 27(3):642–649. doi:10.1063/1.864671*
49. ^D. V. Rose, T. C. Genoni, D. R. Welch, T. A. Mehlhorn, J. L. Porter, et al. (2006). *Flute instability growth on a magnetized plasma column. Physics of Plasmas. 13(9):092507. doi:10.1063/1.2349431*
50. a, bAri Le, Adam Stanier, Lin Yin, Blake Wetherton, Brett Keenan, et al. (2023). *Hybrid-VPIC: An open-source kinetic/fluid hybrid particle-in-cell code. Physics of Plasmas. 30(6):063902. doi:10.1063/5.0146529*
51. a, b, cK. J. Bowers, B. J. Albright, L. Yin, B. Bergen, T. J. T. Kwan. (2008). *Ultrahigh performance three-dimensional electromagnetic relativistic kinetic plasma simulationa). Physics of Plasmas. 15(5):055703. doi:10.1063/1.2840133*
52. ^Tony Qian, Jay K. Anderson, Douglass Endrizzi, Cary B. Forest, Jonathan D. Pizzo, et al. (2023). *Experimental Plans for MHD Stability in WHAM. In: APS division of plasma physics meeting abstracts. p. UP11.00077. (APS meeting abstracts; vol. 2023).*
53. ^Yu V. Petrov, R. W. Harvey. (2016). *A fully-neoclassical finite-orbit-width version of the CQL3D Fokker-Planck code. Plasma Physics and Controlled Fusion. 58(11):115001. doi:10.1088/0741-3335/58/11/115001*
54. ^Ethan E. Peterson. (2019). *A Laboratory Model for Magnetized Stellar Winds. PhD thesis, University of Wisconsin, Madison.*
55. a, b, cS. J. Frank, J. Viola, Yu. V. Petrov, J. K. Anderson, D. Bindl, et al. (2024). *Integrated modelling of equilibrium and transport in axisymmetric magnetic mirror fusion devices. arXiv e-prints. :arXiv:2411.06644. doi:10.48550/arXiv.2411.06644*
56. ^Wael R. Elwasif, David E. Bernholdt, Aniruddha G. Shet, Samantha S. Foley, Randall Bramley, et al. (2010). *The design and implementation of the SWIM integrated plasma simulator. In: Marco Danelutto, Julien Bourgeois, Tom Grosseditors. Proceedings of the 18th euromicro conference on parallel, distributed and network-based processing.: IEEE; Computer Society Press pp. 419–427. doi:10.1109/PDP.2010.63*
57. ^Igor Kotelnikov. (2024). *On the stability of the m=1 rigid ballooning mode in a mirror trap with high-beta sloshing ions. arXiv e-prints. :arXiv:2406.10488. doi:10.48550/arXiv.2406.10488*
58. ^B. A. Wetherton, A. Le, J. Egedal, C. Forest, W. Daughton, et al. (2021). *A drift kinetic model for the expander region of a magnetic mirror. Physics of Plasmas. 28(4):042510. doi:10.1063/5.0044160*

59. ^G. N. Watson. (1922). *A Treatise on the Theory of Bessel Functions.* Cambridge University Press.

60. ^Evan L. Yerger, Matthew W. Kunz, Archie F. A. Bott, Anatoly Spitkovsky. (2024). *Collisionless conduction in a high-beta plasma: a collision operator for whistler turbulence.* arXiv e-prints. :arXiv:2405.06481. doi:10.48550/arXiv.2405.06481

61. ^A. A. Ivanov, V. V. Prikhodko. (2017). *Gas dynamic trap: experimental results and future prospects.* Physics Uspekhi. 60(5):509. doi:10.3367/UFNe.2016.09.037967

62. ^C. F. Kennel, H. E. Petschek. (1966). *Limit on Stably Trapped Particle Fluxes.* 71:1. doi:10.1029/JZ071i001p00001

63. ^B. G. Logan, J. F. Clauser, F. H. Coensgen, D. L. Correl, W. F. Cummins, et al. (1976). *High-β, Gas-Stabilized, Mirror-Confined Plasma.* 37(22):1468–1471. doi:10.1103/PhysRevLett.37.1468

64. ^Alexei D. Beklemishev, Peter A. Bagryansky, Maxim S. Chaschin, Elena I. Soldatkina. (2010). *Vortex Confinement of Plasmas in Symmetric Mirror Traps.* Fusion Science and Technology. 57(4):351–360. doi:10.13182/FST10-A9497

65. ^D. V. Yakovlev, A. G. Shalashov, E. D. Gospodchikov, V. V. Maximov, V. V. Prikhodko, et al. (2018). *Stable confinement of high-electron-temperature plasmas in the GDT experiment.* Nuclear Fusion. 58(9):094001. doi:10.1088/1741-4326/aacb88

66. ^M. Yoshikawa, J. Kohagura, R. Ikezoe, M. Sakamoto, N. Ezumi, et al. (2019). *Suppression of flute-like fluctuation by potential formation in GAMMA 10/PDX.* Nuclear Fusion. 59(7):076031. doi:10.1088/1741-4326/ab160d

67. a, bR. F. Post. (1987). *The magnetic mirror approach to fusion.* Nuclear Fusion. 27(10):1579.

68. ^B. B. Kadomtsev, A. B. Mikhailovskii, A. V. Timofeev. (1964). *Negative Energy Waves in Dispersive Media.* Sov Phys JETP. 20(6):1517.

69. ^Abraham Bers, Sheldon Gruber. (1965). *Negative-Energy Plasma Waves and Instabilities at Cyclotron Harmonics.* Applied Physics Letters. 6(2):27–28. doi:10.1063/1.1728231

70. ^Mark E. Koepke. (1992). *Effects of bounce-resonance damping on the harmonics of a plasma microinstability.* Physics of Fluids B. 4(5):1193–1198. doi:10.1063/1.860127

71. a, bK. V. Roberts, J. B. Taylor. (1962). *Magnetohydrodynamic Equations for Finite Larmor Radius.* 8(5):197–198. doi:10.1103/PhysRevLett.8.197

72. ^D. D. Ryutov, H. L. Berk, B. I. Cohen, A. W. Molvik, T. C. Simonen. (2011). *Magneto-hydrodynamically stable axisymmetric mirrorsa).* Physics of Plasmas. 18(9):092301. doi:10.1063/1.3624763

73. ^*M. N. Rosenbluth, N. A. Krall, N. Rostoker. (1962). Finite Larmor Radius Stabilization of "Weakly" Unstable Confined Plasmas. In: Nuclear fusion: 1962 supplement, part 1.*
74. ^*M. Ichimura, M. Inutake, R. Katsumata, N. Hino, H. Hojo, et al. (1993). Relaxation of pressure anisotropy due to Alfvén-ion-cyclotron fluctuations observed in ion-cyclotron-range-of-frequency-heated mirror plasmas. 70(18):2734–2737. doi:10.1103/PhysRevLett.70.2734*
75. ^*R. Katsumata, M. Ichimura, M. Inutake, H. Hojo, A. Mase, et al. (1996). Eigenmode excitation of Alfvén ion cyclotron instability. Physics of Plasmas. 3(12):4489–4495. doi:10.1063/1.872067*
76. ^*S. Peter Gary, Michael E. McKean, Dan Winske, Brian J. Anderson, Richard E. Denton, et al. (1994). The proton cyclotron instability and the anisotropy/β inverse correlation. 99(A4):5903–5914. doi:10.1029/93JA03583*
77. ^*Petr Hellinger, Pavel Trávníček, Justin C. Kasper, Alan J. Lazarus. (2006). Solar wind proton temperature anisotropy: Linear theory and WIND/SWE observations. 33(9):L09101. doi:10.1029/2006GL025925*
78. ^*Philip A. Isenberg, Bennett A. Maruca, Justin C. Kasper. (2013). Self-consistent Ion Cyclotron Anisotropy-Beta Relation for Solar Wind Protons. 773(2):164. doi:10.1088/0004-637X/773/2/164*
79. ^*Yu. A. Tsidulko, I. S. Chernoshtanov. (2014). Alfvén ion-cyclotron instability in an axisymmetric trap with oblique injection of fast atoms. Plasma Physics Reports. 40(12):955–964. doi:10.1134/S1063780X1412006X*
80. ^*T. Tajima, K. Mima, J. M. Dawson. (1977). Alfvén Ion-Cyclotron Instability: Its Physical Mechanism and Observation in Computer Simulation. 39(4):201–204. doi:10.1103/PhysRevLett.39.201*
81. ^*T. Tajima, K. Mima. (1980). Stabilization of the Alfvén-ion cyclotron instability in inhomogeneous media. Physics of Fluids. 23(3):577–589. doi:10.1063/1.863007*
82. ^*B. S. Nicks, S. Putvinski, T. Tajima. (2023). Stabilization of the Alfvén-ion cyclotron instability through short plasmas: Fully kinetic simulations in a high-beta regime. Physics of Plasmas. 30(10):102108. doi:10.1063/5.0163889*
83. ^*J. K. Anderson, O. Anderson, T. M. Biewer, B. Biswas, M. R. Brown, et al. (2024). First physics results from the wisconsin HTS axisymmetric mirror (WHAM). In: APS division of plasma physics meeting abstracts. p. ZI03.00001. (APS meeting abstracts; vol. 2024).*
84. a, b*Thomas H. Stix. (1992). Waves in Plasmas. Melville, New York: American Institute of Physics.*
85. ^*E. G. Harris. (1959). Unstable Plasma Oscillations in a Magnetic Field. 2(2):34–36. doi:10.1103/PhysRevLett.2.34*

86. ^Donald A. Gurnett, Amitava Bhattacharjee. (2017). Introduction to Plasma Physics. Second. Cambridge University Press.
87. ^Gerry McCartney, Thomas Hacker, Baijian Yang. (2014). Empowering Faculty: A Campus Cyberinfrastructure Strategy for Research Communities. Educause Review. Available from: https://er.educause.edu/articles/2014/7/empowering-faculty-a-campus-cyberinfrastructure-strategy-for-research-communities
88. ^X. Carol Song, Preston Smith, Rajesh Kalyanam, Xiao Zhu, Eric Adams, et al. (2022). Anvil - system architecture and experiences from deployment and early user operations. In: Practice and experience in advanced research computing 2022: Revolutionary: Computing, connections, you.: New York, NY, USA: Association for Computing Machinery. (PEARC '22). doi:10.1145/3491418.3530766
89. ^Center for High Throughput Computing. Center for high throughput computing. Center for High Throughput Computing 2006. doi:10.21231/GNT1-HW21
90. ^Timothy J. Boerner, Stephen Deems, Thomas R. Furlani, Shelley L. Knuth, John Towns. (2023). ACCESS: Advancing innovation: NSF's advanced cyberinfrastructure coordination ecosystem: Services & support. In: Practice and experience in advanced research computing.: New York, NY, USA: Association for Computing Machinery pp. 173–176. (PEARC '23). doi:10.1145/3569951.3597559
91. ^A. Stanier, L. Chacón, G. Chen. (2019). A fully implicit, conservative, non-linear, electromagnetic hybrid particle-ion/fluid-electron algorithm. Journal of Computational Physics. 376:597–616. doi:10.1016/j.jcp.2018.09.038

Declarations

Funding: Funding for this work was provided by Realta Fusion, the U.S. Department of Energy (DOE), and the U.S. National Science Foundation (NSF). WHAM collaboration work is supported by the U.S. DOE through ARPA-E DE-AR0001258, Commonwealth Fusion Systems, Realta Fusion, Wisconsin Alumni Research Foundation, and a lengthy list of collaborators providing valuable equipment. AT was partly supported by NSF PHY-2010189 and the DOE Fusion Energy Sciences Postdoctoral Research Program, administered by the Oak Ridge Institute for Science and Education (ORISE) and Oak Ridge Associated Universities (ORAU) under DOE contract DE-SC0014664. High-performance computing resources were provided by the National Energy Research Scientific Computing Center (NERSC), a DOE Office of Science User Facility, via allocation FES-ERCAP0026655; Anvil at Purdue University's Rosen

Center for Advanced Computing[84][85] via allocation PHY230179 from the NSF Advanced Cyberinfrastructure Coordination Ecosystem: Services & Support (ACCESS) program; Amazon Web Services' Compute for Climate Fellowship awarded to Realta Fusion; Los Alamos Institutional Computing; and UW–Madison's Center for High Throughput Computing[86]. ACCESS[87] is supported by NSF grants #2138259, #2138286, #2138307, #2137603, and #2138296. All opinions expressed in this paper are the authors' and do not necessarily reflect the policies and views of DOE, ORAU, or ORISE.

Potential competing interests: C. B. Forest is a co-founder of Realta Fusion; D. A. Endrizzi, S. J. Frank, and J. Viola are employees of Realta Fusion. This work was partly supported by a grant from Realta Fusion to the University of Wisconsin–Madison.

doi.org/10.32388/6MKS9W